

A Determination of the Top Mass from a Global PDF Analysis

Richard D. Ball,^a Jaco ter Hoeve,^a Roy Stegeman^{a,b}

^a*The Higgs Centre for Theoretical Physics, University of Edinburgh,
JCMB, KB, Mayfield Rd, Edinburgh EH9 3FD, Scotland*

^b*Quantum Research Centre, Technology Innovation Institute, Abu Dhabi, UAE*

E-mail: r.d.ball@ed.ac.uk, jaco.ter.hoeve@ed.ac.uk,
r.stegeman@ed.ac.uk

ABSTRACT: We present an indirect determination of the top-quark pole mass m_t within a global analysis of parton distribution functions (PDFs), based on the public NNPDF framework. We consider a wide range of single- and double-differential top cross-section measurements, and compare them to theoretical predictions computed at NNLO QCD accuracy with EW corrections, analysing their individual as well as combined impact on the joint (α_s, m_t) parameter space, while accounting for PDF evolution up to approximate N³LO QCD accuracy with QED corrections. We account for missing higher order QCD uncertainties by default. Unique to our analysis are the inclusion of, first, toponium contributions around the $t\bar{t}$ threshold, second, state-of-the-art constraints on α_s from the lattice, and finally, a detailed sensitivity study of the various ATLAS and CMS differential cross-section measurements at 8 and 13 TeV. We demonstrate explicitly how a combined determination requires the refitting of the PDFs in order to correctly correlate uncertainties. We find $m_t = 172.80 \pm 0.26$ GeV at approximate N³LO QCD including NLO QED, EW and toponium corrections.

Contents

1	Introduction	1
2	Methodology	3
2.1	The theory covariance method	3
2.2	Closure test methodology	6
3	Experimental data and theoretical predictions	7
3.1	Experimental measurements	7
3.2	Theory settings	9
3.3	Toponium corrections	11
4	Results	14
4.1	Closure test results	15
4.2	Determining m_t and $\alpha_s(m_Z)$ at NNLO	16
4.3	Impact of other small corrections	24
4.4	Comparison to other determinations of the top mass	29
5	Summary and outlook	32
A	Toponium k-factors	34

1 Introduction

The top quark is the heaviest known particle in the Standard Model (SM) and is copiously produced at the LHC. In Run II alone, the ATLAS and CMS collaborations have collected an impressive number of $t\bar{t}$ cross-section measurements, ranging from total cross sections [1–6], to single [7–12], double [8, 9] and even triple [13, 14] differential measurements. Run III, operating at $\sqrt{s} = 13.6$ TeV, has already collected as much luminosity as all of Run II combined, and first results are starting to become available [15, 16]. This large data set enables an increasingly precise determination of the top quark pole mass, m_t , with a current PDG average of $m_t = 172.4 \pm 0.7$ GeV [17], see Ref. [18] for a review.

An accurate and precise determination of the top quark pole mass is relevant for several reasons. It provides a key input parameter to many processes at the LHC, and therefore tests the internal consistency of the SM [19, 20]. Moreover, being the heaviest SM particle, it couples most strongly to the Higgs-boson and thus provides a promising avenue to search for possible BSM effects [21, 22]. It also plays an important role, together with the strong coupling constant $\alpha_s(m_Z)$, in determining whether the universe resides in a meta-stable or stable state through the running of the quartic Higgs self-coupling [23–26].

Following the discovery of the top quark at the Tevatron [27, 28], the ATLAS and CMS collaborations have performed a series of direct measurements of its mass [29–37], of which $m_t = 172.95 \pm 0.53$ [36] and $m_t = 171.77 \pm 0.37$ GeV [33] provide the most precise direct determinations from a single channel. The combination of ATLAS and CMS measurements up to run-I resulted in a precision of $m_t = 172.52 \pm 0.33$ GeV [38]. Looking beyond, High-Luminosity LHC (HL-LHC) projections currently predict a sub-GeV precision of 200 MeV [39], which might be further improved by future electron-positron colliders to a precision of $\mathcal{O}(10)$ MeV [40].

In recent years, several groups outside the experimental collaborations have performed determinations of m_t from top production cross-sections, differing in terms of experimental datasets, higher orders in the perturbative QCD expansion, and methodologies [41–47]. Given that top cross-sections depend not only on m_t , but also on α_s and the parton distribution functions (PDFs), which themselves also depend strongly on α_s , an accurate determination of m_t from top cross-sections ideally requires a joint determination of all these quantities in the context of a global fit. This is necessary to capture all the correlations in the $(m_t, \alpha_s, \text{PDF})$ parameter space: failing to take full account of such correlations can lead to biases [48, 49].

The NNPDF collaboration recently performed a global determination of α_s from hadronic data, with a fixed value of m_t [50, 51]. This determination was performed using the theory covariance method (TCM) [52–55], which enables accurate and efficient determination of discrete parameters such as α_s within the context of a global fit to PDFs, accounting for all correlations. The aim of this paper is to likewise use the TCM to provide an accurate determination of the top pole mass, m_t , while accounting for all correlations with $\alpha_s(m_Z)$ and the PDFs in the context of a global fit. We adopt state-of-the-art NNLO theoretical predictions of $t\bar{t}$ production cross-sections, complemented with EW corrections, and benefit from the wide range of experimental measurements included in NNPDF4.0 [56], supplemented with several new $t\bar{t}$ measurements that have become available since its release. We study in detail the sensitivity to m_t to the various differential observables determined from the experimental datasets, and explicitly demonstrate how their accurate combination can only be performed in the context of the global PDF fit. For the first time, to the best of our knowledge, we also analyse how toponium corrections [57, 58] affect the extraction of m_t .

The structure of this paper is as follows. First, Sect. 2 sets out the application of the Theory Covariance Method to the problem at hand. Sect. 3 then describes the experimental datasets and corresponding theoretical predictions that we use in our fit. Here we also discuss how we model and account for (possible) toponium corrections. Sect. 4 presents the main results of our determination, first validating our methodology in a controlled setup by means of a closure test, followed by a demonstration of the impact of higher order perturbative corrections. We also comment on how our results compare to previous results. Finally, we conclude and summarise in Sect. 5.

2 Methodology

2.1 The theory covariance method

We start by reviewing the methodological framework that we adopt throughout this work to extract m_t alongside $\alpha_s(m_Z)$ from a global PDF fit. Our methodology makes use of the theory covariance matrix formalism [52–54] used to account for theoretical uncertainties in PDF fits, and the Theory Covariance Method (TCM) [55] which enables an analytical extraction of the underlying nuisance parameters. The TCM was originally developed to determine the correlations between theoretical uncertainties entering PDF fits and predictions made using these PDFs, but it can equally be used to optimise external physical parameters in the context of a PDF fit, as demonstrated explicitly in the case of $\alpha_s(m_Z)$ in Ref. [50]. The advantages of the TCM with respect to alternative methods are threefold: since the parameter extraction is analytic, as opposed to numerical, it does not interfere with the subtleties of the PDF extraction (in particular the cross-validation and stopping required because the PDFs are continuous functions); the covariance matrix of the parameters is determined without the need for a $\Delta\chi^2$ criterion, avoiding the tolerance ambiguities inherent in Hessian methods; the TCM is numerically accurate and efficient, requiring only a single PDF fit (as opposed to the multiple fits needed in the correlated replica method [59]), and as a result it makes it possible to extract any number of correlated external parameters simultaneously, without the need for exceptional computational resources. In this section we will show how the TCM can be applied to the special case of extracting two correlated physical parameters, the pole mass m_t together with the strong coupling $\alpha_s(m_Z)$, in the context of a global PDF fit.

To this end, consider n_{dat} Gaussian distributed measurements $D = (D_1, \dots, D_{n_{\text{dat}}})^T$ (so D is a column vector, while D^T is a row vector), with covariance matrix C in the space of the data, and the corresponding theoretical predictions $T = (T_1, \dots, T_{n_{\text{dat}}})^T$. Theory uncertainties may be modelled by introducing univariate Gaussian nuisance parameters λ_a centered around zero,

$$P(\lambda) \propto \exp\left[-\frac{1}{2}\lambda_a^2\right], \quad (2.1)$$

whose effect is to smear out the vector of theory predictions T by vectors β_a , such that the conditional probability of T is given by

$$P(T|D\lambda) \sim \exp\left[-\frac{1}{2}(T + \lambda_a\beta_a - D)^T C^{-1}(T + \lambda_a\beta_a - D)\right], \quad (2.2)$$

where the summation over the index a , labelling the nuisance parameters, is left implicit. It is straightforward to show that the introduction of the nuisance parameters λ_a in Eq. (2.2) is equivalent to adding a contribution $\beta_a\beta_a^T$ to the original covariance matrix C . Adopting a Bayesian framework, the probability $P(T|D)$ can be obtained by marginalising $P(T|D\lambda)$ over λ ,

$$P(T|D) = \int d\lambda P(T|D\lambda)P(\lambda), \quad (2.3)$$

which after completing the square in λ leads to,

$$P(T|D) \propto \exp \left[-\frac{1}{2}(T - D)^T (C + S)^{-1} (T - D) \right], \quad (2.4)$$

with $S = \beta_a \beta_a^T$. Therefore, theoretical uncertainties can be accounted for simply by adding to the original covariance matrix C an additional contribution S .

Moreover, we can also use Bayes' theorem to find the posterior distribution of the λ_a :

$$P(\lambda|TD) \propto \exp \left[-\frac{1}{2}(\lambda_a - \bar{\lambda}_a) Z_{ab}^{-1} (\lambda_b - \bar{\lambda}_b) \right], \quad (2.5)$$

where

$$\bar{\lambda}_a = \beta_a^T (C + S)^{-1} (D - T), \quad (2.6)$$

$$Z_{ab} = \delta_{ab} - \beta_a^T (C + S)^{-1} \beta_b, \quad (2.7)$$

denote the posterior mean and covariance of λ_a , respectively. Next we consider some new theoretical prediction \tilde{T} that has not been fitted to D , although its theory uncertainties are fully correlated to those of T (such that $\tilde{\lambda}_a = \lambda_a$), that is,

$$\tilde{T}(\lambda) = \tilde{T} + \lambda_a \tilde{\beta}_a. \quad (2.8)$$

Using Eq. (2.6) we find that the posterior distribution on λ_a induces a shift $\delta\tilde{T}$ with respect to the prior central value \tilde{T} ,

$$\delta\tilde{T} = \hat{S} (C + S)^{-1} (D - T), \quad (2.9)$$

where we have defined $\hat{S} \equiv \tilde{\beta}_a \beta_a^T$ as the cross-covariance between the theoretical predictions entering the fit and the new predictions \tilde{T} . Defining $\tilde{S} \equiv \tilde{\beta}_a \tilde{\beta}_a^T$ as the prior theoretical covariance on \tilde{T} , the posterior covariance on \tilde{T} can be straightforwardly obtained from Eq. (2.7) as

$$\text{Cov}[\tilde{T}] \equiv \tilde{S} - \hat{S} (C + S)^{-1} \hat{S}^T. \quad (2.10)$$

Note how the prior theoretical covariance \tilde{S} is reduced by the second term in Eq. (2.10), an example of statistical learning.

Let us now apply the above to the NNPDF methodology for determining the PDFs [56, 60]. Rather than fitting T directly to D , here we construct first N_{rep} data replicas $D^{(r)}$ drawn from a Gaussian distribution centered around the experimental data D with covariance $C + S$,

$$D^{(r)} \sim \mathcal{N}(D, C + S), \quad (2.11)$$

from which we then determine a corresponding theory replica $T^{(r)}$ by optimising (through cross-validation) the following figure of merit as a function of the PDFs f ,

$$\chi_r^2[f] = (T^{(r)}[f] - D^{(r)})^T (C + S)^{-1} (T^{(r)}[f] - D^{(r)}). \quad (2.12)$$

While optimising Eq. (2.12) m_t and $\alpha_s(m_Z)$ are kept fixed at the prior central values

m_t^0 and α_s^0 . We assume prior uncertainties Δm_t and $\Delta \alpha_s$, and define $m_t^\pm = m_t^0 \pm \Delta m_t$, $\alpha_s^\pm = \alpha_s^0 \pm \Delta \alpha_s$. We then define four nuisance parameters as the allowable upward and downward variation of these two observables, as permitted by the PDF fit.

We can now construct the vectors β_a , $a = 1, \dots, 4$, and thus the three matrices S , \hat{S} and \tilde{S} . We define $T^{(0)} \equiv \langle T^{(r)} \rangle$ as the central theory predictions obtained by taking the average over the replicas r . The vectors β_a are constructed from four sets of shifts ΔT^\pm with respect to the central theory predictions $T^{(0)}$ induced by varying α_s and m_t around their prior central values (we choose four rather than two because the theory predictions are not necessarily linear in the external parameters):

$$\Delta T_{m_t}^\pm \equiv T^{(0)}(m_t^\pm) - T^{(0)}(m_t^0), \quad (2.13)$$

$$\Delta T_{\alpha_s}^\pm \equiv T^{(0)}(\alpha_s^\pm) - T^{(0)}(\alpha_s^0), \quad (2.14)$$

and construct β_a in terms of these,

$$\beta_a = \frac{1}{\sqrt{2}} \left(\Delta T_{m_t}^+, \Delta T_{m_t}^-, \Delta T_{\alpha_s}^+, \Delta T_{\alpha_s}^- \right). \quad (2.15)$$

Recalling that $S = \beta_a \beta_a^T$, we thus find for the prior covariance of the theory predictions

$$S_{ij} = \frac{1}{2} \left(\Delta T_{m_t,i}^+ \Delta T_{m_t,j}^+ + \Delta T_{m_t,i}^- \Delta T_{m_t,j}^- + \Delta T_{\alpha_s,i}^+ \Delta T_{\alpha_s,j}^+ + \Delta T_{\alpha_s,i}^- \Delta T_{\alpha_s,j}^- \right), \quad (2.16)$$

where we have displayed the indices in data space explicitly, for clarity.

Our two parameters to be predicted are $\tilde{T}(\lambda) = (m_t, \alpha_s)^T$, so we recast Eq. (2.8) as

$$\tilde{T} = \begin{pmatrix} m_t^0 + \lambda_{m_t^+} \Delta m_t - \lambda_{m_t^-} \Delta m_t \\ \alpha_s^0 + \lambda_{\alpha_s^+} \Delta \alpha_s - \lambda_{\alpha_s^-} \Delta \alpha_s \end{pmatrix}, \quad (2.17)$$

where $\lambda_{m_t^\pm}$ and $\lambda_{\alpha_s^\pm}$ are the four nuisance parameters, to be determined replica by replica in the PDF fit optimising Eq. (2.12). Then

$$\tilde{\beta}_a = \frac{1}{\sqrt{2}} \begin{pmatrix} \Delta m_t, -\Delta m_t, 0, 0 \\ 0, 0, \Delta \alpha_s, -\Delta \alpha_s \end{pmatrix}, \quad (2.18)$$

and thus $\tilde{S} = \tilde{\beta}_a \tilde{\beta}_a^T$ while $\hat{S} = \tilde{\beta}_a \beta_a^T$,

$$\tilde{S} = \begin{pmatrix} \Delta m_t^2 & 0 \\ 0 & \Delta \alpha_s^2 \end{pmatrix}, \quad \hat{S}_i = \frac{1}{2} \begin{pmatrix} (\Delta T_{m_t,i}^+ - \Delta T_{m_t,i}^-) \Delta m_t \\ (\Delta T_{\alpha_s,i}^+ - \Delta T_{\alpha_s,i}^-) \Delta \alpha_s \end{pmatrix}. \quad (2.19)$$

Following similar steps that led to Eq. (2.9), the prior central values $\tilde{T} = (m_t^0, \alpha_s^0)^T$ thus undergo the following net shifts

$$\delta \tilde{T} = \hat{S} (C + S)^{-1} (D - T^{(0)}). \quad (2.20)$$

The associated covariance Eq. (2.10) now receives an additional contribution arising from

fluctuations of the replicas, corresponding to the PDF uncertainty:

$$\text{Cov}[\tilde{T}] = \tilde{S} - \hat{S}(C + S)^{-1}\hat{S}^T + \hat{S}(C + S)^{-1}X(C + S)^{-1}\hat{S}^T, \quad (2.21)$$

where X is the covariance matrix of the optimal theory predictions determined by the fit,

$$X_{ij} \equiv \langle (T_i^{(r)} - T_i^{(0)})(T_j^{(r)} - T_j^{(0)}) \rangle, \quad (2.22)$$

the average again being over the replicas. The contribution from the PDF uncertainty is positive, because the necessity to use much of the data to determine the PDFs necessarily reduces the predictive power of the data in the determination of the external parameters.

Note that in the case of a theory which always gives a perfect fit, that is $T = D$ for all replicas, we would have $X = C + S$ and Eq. (2.21) reduces to the prior uncertainty \tilde{S} . This is because in that case all information contained in the data is absorbed completely by the theory, leaving no room to inform the nuisance parameters so that the posterior can only coincide with the prior. In practice, a theory like the Standard Model is highly constraining, and thus cannot always fit data fluctuations exactly, leaving sufficient wiggle room to update the external parameters. In a sense this is what we mean by a predictive theory, as opposed to a purely phenomenological one.

Regarding the prior uncertainties on $\alpha_s(m_Z)$ and m_t , we choose sensible values to give a distribution wide enough that the final results are independent of the prior, but not so wide as to make the dependence of the theory predictions nonlinear. In practice, we typically take $\Delta m_t = 2.5$ GeV, $\Delta \alpha_s = 0.002$, motivated by the fact that this comfortably encloses uncertainties in the PDG average [17].

2.2 Closure test methodology

Before applying the TCM from Sect. 2.1 to real data, one must first verify whether it is free from any methodological bias by means of a closure test [56, 61–64]. In this approach, synthetic datasets are first generated from a known underlying law $T^* \equiv T(\alpha_s^*, m_t^*, f^*)$ with chosen values α_s^* and m_t^* , and a fixed PDF f^* , and with a covariance $C + S$. The TCM methodology is then applied on each of the synthetic data sets, producing a series of best-fit α_s and m_t values that should be statistically compatible with the true underlying values if the closure test is successful.

In particular, one generates N_{L_1} replicas $D_{L_1}^{(k)}$ drawn from a Gaussian distribution centred around T^* with covariance $C + S$,

$$D_{L_1}^{(k)} \sim \mathcal{N}(T^*, C + S), \quad k = 1, \dots, N_{L_1}, \quad (2.23)$$

where the k^{th} replica $D_{L_1}^{(k)}$ corresponds to the experimental central value one would obtain if one were to imagine performing repeated “runs of the universe”, each time observing a different sample of central values. In the standard NNPDF methodology the uncertainties are propagated by bootstrapping the experimental data, for this reason we introduce a second

level of noise, denoted L_2 , and draw N_{L_2} replicas, this time from each of the L_1 -replicas,

$$D_{L_2}^{(k,r)} \sim \mathcal{N}\left(D_{L_1}^{(k)}, C + S\right), \quad r = 1, \dots, N_{L_2}, \quad (2.24)$$

Then, for each k , we perform a fit following the methodology from Sect. 2 to end up with pairs $\tilde{T}^{(k)} \equiv (m_t^{(k)}, \alpha_s^{(k)})$, each with corresponding covariance $\text{Cov}[m_t^{(k)}, \alpha_s^{(k)}]$. The weighted average of the collection of pairs is then given by

$$\langle(m_t, \alpha_s)\rangle = \left(\sum_{k=1}^{N_{L_1}} \text{Cov}^{-1}[m_t^{(k)}, \alpha_s^{(k)}]\right)^{-1} \left(\sum_{k=1}^{N_{L_1}} \text{Cov}^{-1}[m_t^{(k)}, \alpha_s^{(k)}] \cdot \tilde{T}^{(k)}\right), \quad (2.25)$$

with covariance,

$$\text{Cov}[\langle(m_t, \alpha_s)\rangle] \equiv \left(\sum_k \text{Cov}^{-1}[m_t^{(k)}, \alpha_s^{(k)}]\right)^{-1}. \quad (2.26)$$

For a successful closure test, Eqs. (2.25) and (2.26) must be statistically compatible with the true underlying values α_s^* and m_t^* . The results of such a closure test will be presented in Sect. 4.1.

3 Experimental data and theoretical predictions

In this Section, we describe the experimental data and corresponding theoretical predictions that enter our analysis. We take the NNPDF4.0 data set as our baseline [56], complemented wherever possible with new $t\bar{t}$ production data sets that have become available since its release. Single top data are not included in this study. In the following, we therefore focus exclusively on $t\bar{t}$ cross-section data and refer to Ref. [56] for a complete overview regarding all the other processes included in the global extraction of m_t .

3.1 Experimental measurements

Given the wide variety of the top measurements from LHC, it is important to distinguish between what we mean by an experiment, a data set and an observable. We refer to ATLAS and CMS as experiments, and each provides data sets at different centre of mass energies (8 or 13 TeV) and different decay channels (dilepton, lepton + jet, or hadronic). Within each data set we can further distinguish between cross-section measurements differential in different kinematic observables, such as the top invariant mass $m_{t\bar{t}}$, the top transverse momentum p_T^t , top quark rapidities y_t or $y_{t\bar{t}}$, or combinations thereof in the case of double differential distributions. We refer to a measurement collectively as a particular combination of an experiment (ATLAS/CMS), data set (\sqrt{s} and channel) and observable (differential in $m_{t\bar{t}}$, p_T^t , etc.). In general, measurements at different experiments and at different energies and/or channels can be assumed to be independent, but measurements of different observables within the same experiment and data set are not. The latter may thus only enter a global PDF fit simultaneously when their cross-correlation is (publicly) available.

Table 3.1 provides an overview of the $t\bar{t}$ measurements that we consider, where, for each measurement, we indicate the available observables, the number of data points, n_{dat} , the total integrated luminosity, \mathcal{L}_{int} , and its corresponding reference. We use only differential un-normalized observables in this study, and don't include the total cross-section measurements since these are not independent.

Experiment and data set	Observable	n_{dat}	\mathcal{L}_{int} [fb $^{-1}$]	Ref.
ATLAS 13 TeV $t\bar{t}$ all hadr.	$d\sigma/dm_{t\bar{t}}$	9	36.1	[8]
	$d\sigma/d y_{t\bar{t}} $	12		
	$d^2\sigma/dm_{t\bar{t}} d y_{t\bar{t}} $	11		
ATLAS 13 TeV $t\bar{t} \ell + j$	$d\sigma/dm_{t\bar{t}}$	9	36.0	[9]
	$d\sigma/dp_T^t$	8		
	$d\sigma/d y_t $	5		
	$d\sigma/d y_{t\bar{t}} $	7		
	$d^2\sigma/dm_{t\bar{t}} dp_T^t$	15		
ATLAS 8 TeV $t\bar{t} 2\ell$	$d\sigma/dm_{t\bar{t}}$	6	20.2	[10]
	$d\sigma/dy_{t\bar{t}}$	5		
ATLAS 8 TeV $t\bar{t} \ell + j$	$d\sigma/dm_{t\bar{t}}$	7	20.3	[11]
	$d\sigma/dp_T^t$	8		
	$d\sigma/dy_t$	5		
	$d\sigma/dy_{t\bar{t}}$	5		
CMS 13 TeV $t\bar{t} 2\ell$ 138 fb $^{-1}$	$d\sigma/dm_{t\bar{t}}$	7	138.0	[14]
	$d^2\sigma/dm_{t\bar{t}} d y_{t\bar{t}} $	16		
	$d\sigma/dp_T^t$	7		
	$d\sigma/d y_t $	10		
CMS 13 TeV $t\bar{t} 2\ell$	$d\sigma/dm_{t\bar{t}}$	7	35.9	[7]
	$d\sigma/dp_T^t$	6		
	$d\sigma/d y_t $	10		
	$d\sigma/d y_{t\bar{t}} $	10		
CMS 13 TeV $t\bar{t} \ell + j$	$d\sigma/dm_{t\bar{t}}$	15	137.0	[12]
	$d^2\sigma/dm_{t\bar{t}} d y_{t\bar{t}} $	35		
	$d\sigma/dp_T^t$	16		
	$d\sigma/dy_t$	11		
	$d\sigma/dy_{t\bar{t}}$	10		

Table 3.1: Overview of the $t\bar{t}$ measurements considered in the current analysis. For each measurement, we indicate the available observables, the number of data points, n_{dat} , the integrated luminosity, \mathcal{L}_{int} and the corresponding reference.

Specifically, regarding measurements from ATLAS, we include the fully hadronic channel at 13 TeV with a luminosity of 36.1 fb $^{-1}$ [8], single differential in $m_{t\bar{t}}$, the absolute rapidity $|y_{t\bar{t}}|$, and the double-differentially in $(m_{t\bar{t}}, |y_{t\bar{t}}|)$. In the $\ell + j$ channel, we include the 13 TeV measurement at 36.0 fb $^{-1}$ from Ref. [9], single differential in $m_{t\bar{t}}$, p_T^t , $|y_t|$, $|y_{t\bar{t}}|$

and double differential in $(m_{t\bar{t}}, p_T^t)$. At 8 TeV, we include the dilepton measurement from Ref. [10] at an integrated luminosity of 20.2 fb^{-1} , single differential in $m_{t\bar{t}}$ and $y_{t\bar{t}}$. In the $\ell + j$ channel, we include the measurement from Ref. [11] single differential in $m_{t\bar{t}}, p_T^t$ and the rapidities y_t and $y_{t\bar{t}}$.

In the case of CMS, we consider the dilepton measurement based on the full run-II luminosity from Ref. [14], single differential in $m_{t\bar{t}}, p_T^t$, and the (absolute) rapidities y_t and $y_{t\bar{t}}$, and double differential in the pair $(m_{t\bar{t}}, |y_{t\bar{t}}|)$. We also consider the corresponding lower luminosity measurement at 35.9 fb^{-1} from Ref. [7] for those observables that are not available from the full Run-II equivalent. In the $\ell + j$ channel, we include the run-II legacy measurement from Ref. [12] single differential in $m_{t\bar{t}}, p_T^t, y_t$ and $y_{t\bar{t}}$, and double differential in the pair $(m_{t\bar{t}}, |y_{t\bar{t}}|)$. At 8 TeV CMS only provide normalized differential distributions, which we thus do not include.

3.2 Theory settings

For each of the measurements tabulated in Table 3.1, we compute theoretical predictions at NNLO QCD accuracy using MATRIX [65, 66] interfaced to the PINEAPPL fast grid interface [67, 68]. All measurements are therefore analysed at parton level. Following the methodology outlined in Sect. 2, we produce three sets of theoretical predictions, one for each value of the pole mass m_t in the on-shell scheme; the prior central value $m_t^0 = 172.5 \text{ GeV}$, the up variation, $m_t^+ = 175.0 \text{ GeV}$, and the down variation at $m_t^- = 170.0 \text{ GeV}$. This constitutes our prior, as defined in Eq. (2.15), and its variations are motivated by the fact that the PDG average, $m_t = 172.4 \pm 0.7 \text{ GeV}$, falls comfortably inside it [17]. Regarding α_s variations, we produce predictions for our entire data set, so including all non $t\bar{t}$ data, at

$$\alpha_s = \{0.116, 0.117, \dots, 0.124, 0.125\}, \quad (3.1)$$

giving us flexibility to redefine our α_s prior as needed. We have benchmarked our predictions at NNLO against the database `hightea` [69], as well as `MADGRAPH5_AMC@NLO` [70] in the case of NLO QCD, finding perfect agreement within uncertainties in both cases. The renormalisation and factorisation scales are set to $\mu_R = \mu_F = H_T/4$, with H_T the transverse energy of the $t\bar{t}$ event, defined as,

$$H_T \equiv \sqrt{p_{T,t}^2 + (m_t^0)^2} + \sqrt{p_{T,\bar{t}}^2 + (m_t^0)^2}. \quad (3.2)$$

Note that Eq. (3.2) is always evaluated at $m_t = m_t^0$, meaning that we exclusively vary the top mass dependence in the hard scattering, while leaving μ_R and μ_F fixed to Eq. (3.2). In this way, we probe the true parametric dependence on the top mass, separating it from the scale dependence, which we use to estimate missing higher order uncertainties (MHOUs).

While we have made sure that Monte Carlo (MC) uncertainties on the total integrated cross-sections are below 0.2%, which translates into sub-percent precision across all differential bins, the relative uncertainty expressed with respect to the up and down variations $\Delta T_{m_t, i}^\pm$ can be considerably larger, reaching e.g. $\mathcal{O}(10\%)$ in high invariant mass

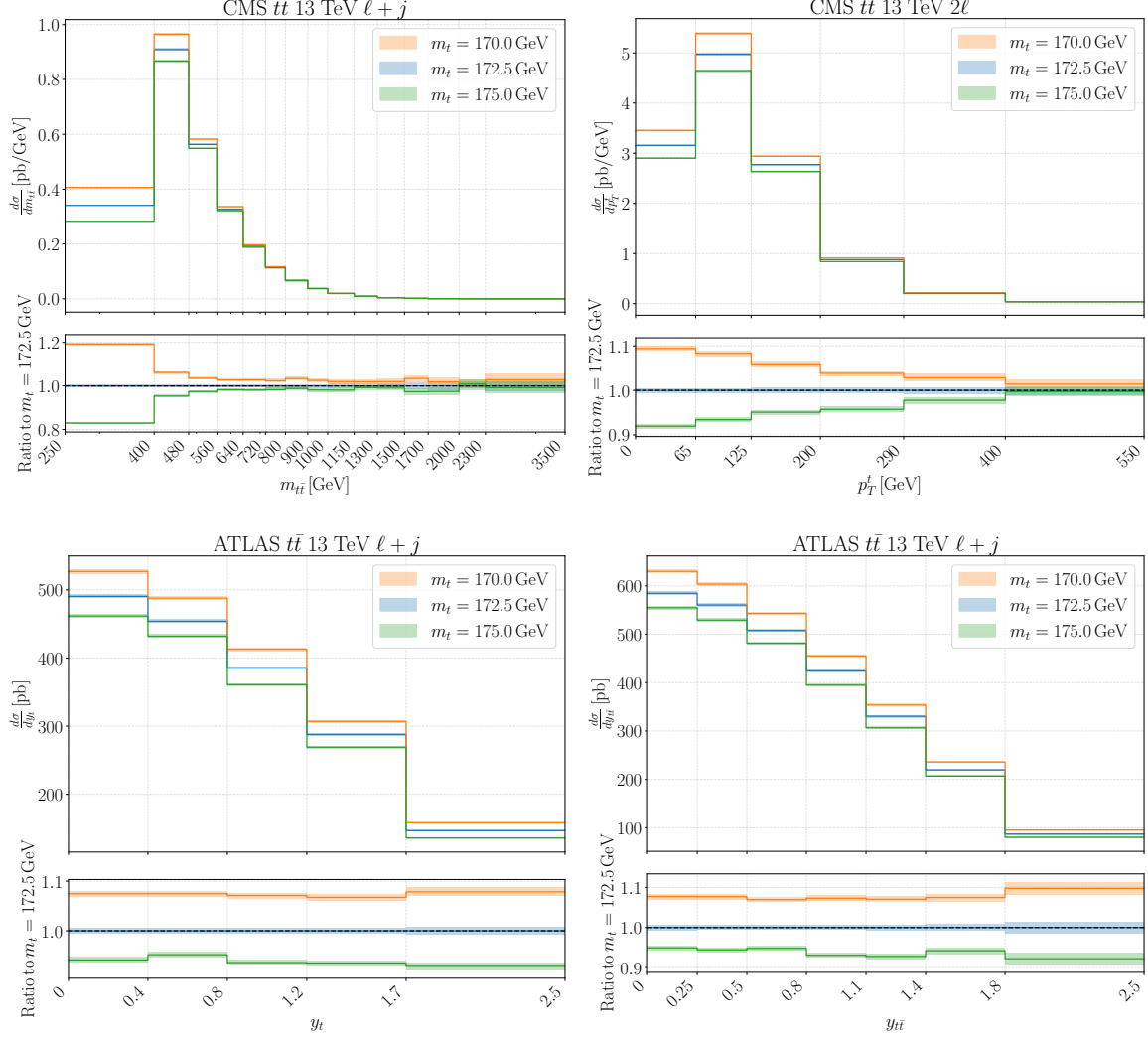


Figure 3.1: Representative differential distributions of $t\bar{t}$ at 13 TeV by ATLAS and CMS at the top-quark pole mass $m_t = \{170.0, 172.5, 175.0\}$ GeV. From top left to bottom right, we show distributions differential in the invariant mass $m_{t\bar{t}}$, the transverse momentum p_T^t , top-quark rapidity y_t and the rapidity $y_{t\bar{t}}$ of the top-quark pair. The shaded bands represent the PDF uncertainties obtained from NNPDF4.0 [56]

bins. To remedy this, we account for MC fluctuations by adding the following (diagonal) contribution to the fit covariance matrix,

$$C_{ij}^{(\text{MC})} = \frac{1}{2} \left((\delta T_{i,m_t}^+)^2 + (\delta T_{i,m_t}^-)^2 \right) \delta_{ij}, \quad (3.3)$$

where $\delta T_{i,m_t}^\pm$ denotes the MC uncertainty on up and downward varied $t\bar{t}$ theory predictions.

It is interesting to visualise how each of the kinematic distributions from Table 3.1 are affected by varying m_t around its nominal value. Fig. 3.1 displays a representative subset of $t\bar{t}$ differential distributions at 13 TeV for $m_t = \{170.0, 172.5, 175.0\}$ GeV. From top left to bottom right, we show distributions in the invariant mass $m_{t\bar{t}}$, the transverse momentum

p_T^t of the top-quark and the rapidities y_t and $y_{t\bar{t}}$. In each case, the shaded colour band represents the PDF uncertainties from the NNPDF40_nnlo_as_01180 PDF set [56]. Several observations can be made by inspecting Fig. 3.1. First, the $m_{t\bar{t}}$ distribution (top left panel) is clearly the most sensitive to m_t , specifically just above the $t\bar{t}$ threshold where variations of up to 20% are observed as indicated in the ratio-plot. At higher invariant masses, however, the shifts drop to below 5% making this region of phase space less sensitive. Similar effects are observed in the p_T^t distribution (top right panel), where m_t variations induce shifts between typically 5% and 10% just above threshold, with only very small shifts at high p_T . A rather different picture emerges in the rapidity distributions shown in the lower panels. Here, no shape effects are observed, i.e. the cross-section shows roughly comparable shifts across all differential bins. We therefore expect the $m_{t\bar{t}}$ and p_T^t distributions to give the most stringent constraints on m_t , with the rapidity distributions being rather less sensitive.

In the following, we always include MHOU's on the theory predictions following Refs. [71, 72] in the 7-point scheme. We adopt the EKO [73, 74] evolution code for PDF evolution, where QED corrections are included following Ref. [75], and aN³LO QCD corrections are implemented according to Ref. [72] complemented with the recent heavy quark matching functions of Ref. [76] and splitting functions of Ref. [77].

For all distributions considered in this work, we compute electroweak corrections using MADGRAPH5_AMC@NLO [70]. Our conventions are similar to those adopted in Ref. [67]. In particular, our NNLO QCD + EW computation includes the $\mathcal{O}(\alpha_s^2)$, $\mathcal{O}(\alpha_s^3)$ and $\mathcal{O}(\alpha_s^4)$ QCD contributions, and the LO $\mathcal{O}(\alpha_s\alpha)$ and NLO $\mathcal{O}(\alpha_s^2\alpha)$ contributions. We do not include the NLO contributions of order $\mathcal{O}(\alpha_s\alpha^2)$, nor the purely EW corrections of order $\mathcal{O}(\alpha^2)$ and $\mathcal{O}(\alpha^3)$. We adopt the same dynamical scale choice as Eq. (3.2) and use the NNPDF40_nlo_as_01180_qed PDF set [56] to include photon initiated channels. Fig. 3.2 displays the impact of the EW corrections expressed relative to the NNLO QCD theory for a representative subset of the $m_{t\bar{t}}$, p_T^t and rapidity distributions from Table 3.1. Similarly to what was argued in Ref. [78], we note how the relative size of the EW corrections depends strongly on the specific kinematic distribution considered, with the largest impact of around -4% observed in the case of the $m_{t\bar{t}}$ and p_T^t distributions, while the rapidity distributions only undergo rescalings at the level of a few per mille.

3.3 Toponium corrections

An intriguing property in $t\bar{t}$ production that has attracted significant interest recently is the formation of toponium just below the top-pair production threshold. This colour-singlet $t\bar{t}$ quasi-bound state was observed independently by the ATLAS and CMS collaborations with an observed cross-section of $9.3_{-1.3}^{+1.4}$ pb and $8.8_{-1.4}^{+1.2}$ pb, respectively [57, 58]. Its effect shows up most notably in the $t\bar{t}$ invariant mass spectrum as a smeared out bump before threshold, where it enhances the $t\bar{t}$ production cross section by around 6.43 pb at $\sqrt{s} = 13$ TeV according to theoretical estimates [79]. This raises the question whether it may have significant impact on the top-quark mass determination, especially given how the latter is predominantly sensitive to the threshold region as observed in Fig. 3.1. Even though its relative contribution to the overall cross-section is below 1% [79], we remark that it can

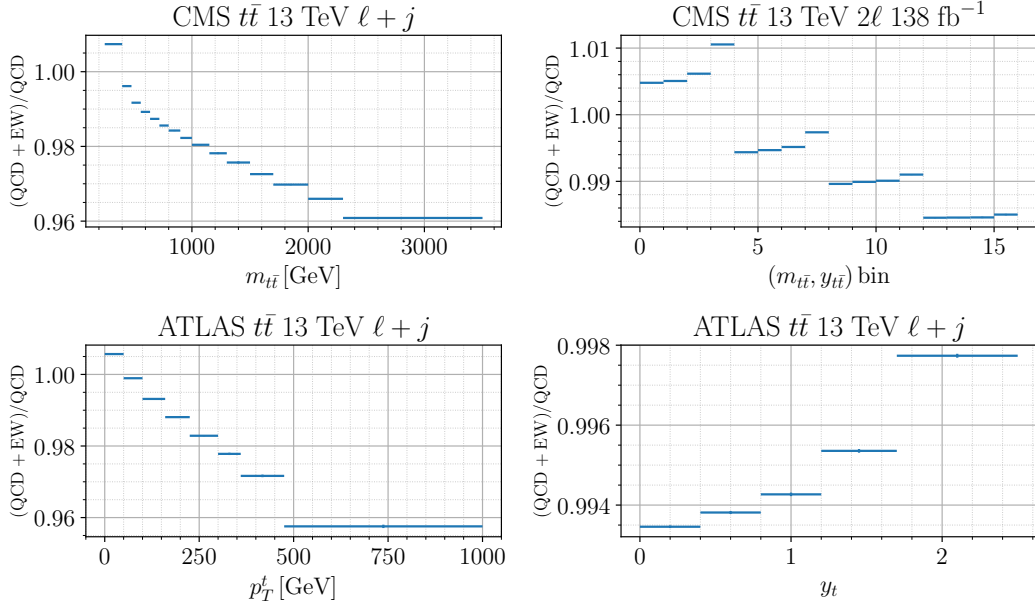


Figure 3.2: Relative EW corrections when considered on top of the NNLO QCD theory for a representative subset of distributions considered in this work. From top left to bottom right, we display the impact in the $m_{t\bar{t}}$ distribution, the double differential distribution in $(m_{t\bar{t}}, y_{t\bar{t}})$, the p_T^t distribution, and the y_t distribution

lead to contributions as high as 6% when considered in isolated bins around threshold, which is clearly significant.

To this end, we account for toponium effects by modelling its contribution through non-relativistic QCD (NRQCD) following the steps outlined in Ref. [80], and as first discussed in Refs. [81, 82]. In particular, we adopt MADGRAPH5_AMC@NLO [70] and generate 100K LO events in the gluon initiated channel,

$$gg \rightarrow t\bar{t} \rightarrow b\ell^+ \nu_\ell \bar{b}\ell'^- \bar{\nu}'_\ell, \quad (3.4)$$

with both top quarks decaying leptonically. As per Ref. [80], we project out the colour singlet contribution to the process in Eq. (3.4) and reweight the corresponding matrix elements \mathcal{M} by the ratio of the respective Green's function in the presence and absence of a tree-level Coulomb potential,

$$|\mathcal{M}|^2 \rightarrow |\mathcal{M}|^2 \left(\left| \frac{\tilde{G}(E; p^*)}{\tilde{G}_0(E; p^*)} \right|^2 - 1 \right), \quad (3.5)$$

where E and p^* denote respectively the toponium's binding energy, and the momentum of the top and anti-top quark viewed from the toponium's rest frame. The -1 term in Eq. (3.5) serves to subtract the LO contribution that is already present in the perturbative SM $t\bar{t}$ events. As remarked in Ref. [80], for $m_{t\bar{t}} > 350$ GeV the average top quark velocity becomes too large to ensure non-relativistic kinematics, and we therefore apply generator-

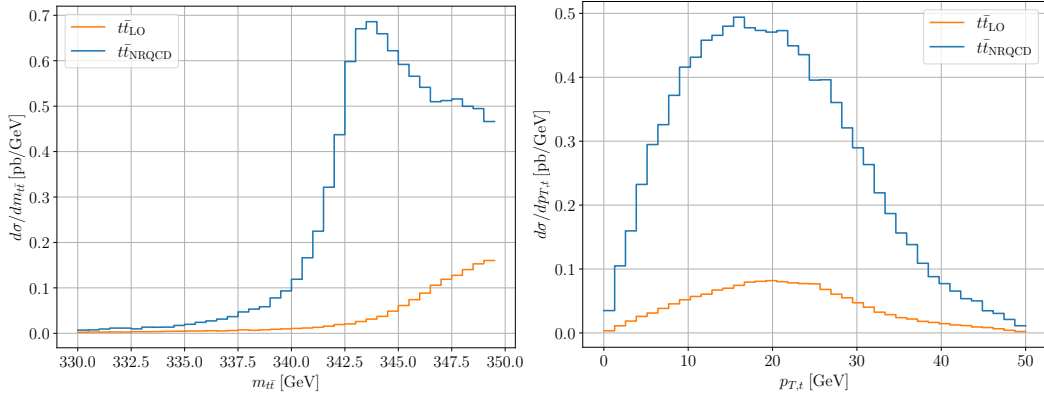


Figure 3.3: Differential distributions in the invariant mass $m_{t\bar{t}}$ (left panel) and top-quark transverse momentum p_T^t (right panel) at LO comparing the toponium signal ($t\bar{t}_{\text{NRQCD}}$) modelled with NRQCD following the reweighting from Eq. (3.5) against the nominal $t\bar{t}$ background at 13 TeV while imposing $m_{t\bar{t}} < 350$ GeV.

level cuts at $m_{t\bar{t}} < 350$ GeV and $p^* < 50$ GeV. Other ways of simulating toponium based on simplified models exist [79, 83], such as through a pseudo-scalar 1S_0 . However, given that these neglect total angular momentum contributions beyond $J = 0$ we shall not consider these further in the current work.

Fig. 3.3 displays the impact of the reweighting according to Eq. (3.5) on the differential cross-section in the invariant mass $m_{t\bar{t}}$ (left panel) and the transverse momentum p_T^t (right panel), comparing the reweighted events, labelled $t\bar{t}_{\text{NRQCD}}$, against the nominal LO QCD background (labelled $t\bar{t}_{\text{LO}}$) when no reweighting is applied. The toponium signal appears most prominently as an increased contribution to the production cross-section around $m_{t\bar{t}} = 2m_t - 2$ GeV, while its effect on p_T^t is limited to relatively low p_T . Its impact on the rapidity distribution rescales all bins uniformly and is therefore not shown. In generating Fig. 3.3, we used the NNPFD40_nn1o_as_01180 PDF set [56] and set the pole mass to $m_t = 172.5$ GeV. We furthermore note that the sample has been rescaled to the total cross sections reported in Table I of Ref. [79] in order to remove the effect of the leptonic branching ratios, to account for the colour-octet contribution to Eq. (3.4), and to allow for a smooth interpolation between the threshold and relativistic region [84].

In order to incorporate the toponium signal into our fit, we include it as an additional contribution to our NNLO cross-section predictions in the absence of toponium as described in Sect. 3.2. In particular, we multiply our NNLO QCD $t\bar{t}$ prediction in bin i without toponium, denoted $T_i^{t\bar{t}}$, by a toponium k -factor,

$$k_i^{(\text{topo})} \equiv 1 + T_i^{t\bar{t}_{\text{NRQCD}}} / T_i^{t\bar{t}} \quad (3.6)$$

where $T_i^{t\bar{t}_{\text{NRQCD}}}$ denotes the toponium contribution obtained from applying the reweighting from Eq. (3.5). The toponium k -factors for the measurements listed in Table 3.1 are provided in App. A.

In this context, it is relevant to point out a subtlety regarding the perturbative match-

ing between the Green’s function method and the fixed order NNLO QCD predictions. As discussed in Refs. [85–88], and more recently in Ref. [89], one needs to be careful not to double count terms that are present in both the perturbative QCD expansion and the resummation of the Coulomb interactions to all orders. Specifically, the latter resums terms in the (α_s/v) expansion, where v denotes the velocity of the top-quark in the toponium’s rest frame, so that the (α_s/v) and $(\alpha_s/v)^2$ contributions already included in the NNLO QCD calculation must be subtracted consistently when combined. A quantitative assessment of the size of this overlap was computed in Ref. [89] in the case of the CMS measurement from Ref. [90], where they predict a cross-section of 0.602 pb/GeV at pure NNLO QCD, while the threshold corrected result comes out slightly higher at 0.661 pb/GeV. Correcting for the bin width then gives a difference between both calculations of 3.54 pb.

Motivated by this theoretical effect, and by the higher values of the toponium cross-section measured by ATLAS and CMS [57, 58], we conservatively assign a fully correlated 50% uncertainty to the toponium k -factor in Eq. (3.6), such that we can accommodate all the various uncertainties within one sigma. This is done by adding a further contribution to the fit covariance matrix,

$$C_{ij}^{(\text{topo})} = \frac{1}{4} T_i^{t\bar{t}_{\text{NRQCD}}} T_j^{t\bar{t}_{\text{NRQCD}}}, \quad (3.7)$$

which has a single non-vanishing eigenvalue as expected for a normalization uncertainty.

4 Results

We now present the main results of this work. First, in Sect. 4.1, we validate our methodology in a controlled setup with synthetic data following the closure testing described in Sect. 2.2. We then move to applications to real data, always including MHOU, presenting first results at NNLO QCD accuracy in Sect. 4.2. Here we also study in detail the impact of different ways of statistically combining multiple measurements. We then study a series of refinements, starting with aN³LO and aN³LO \otimes NLO_{QED} corrections in Sect. 4.3. The impact of toponium corrections are studied in Sect. 4.3, while the impact of constraining the prior on $\alpha_s(m_Z)$ to the recent FLAG determination [91] is presented in Sect. 4.3. We end in Sect. 4.4 by comparing our results to other m_t determinations in the literature.

The fits in this section are all performed in exactly the same way: we choose a global dataset (either real data or, in Sect. 2.2 pseudo-data), including a selection of the available top data, add the theory covariance matrix S computed according to the chosen prior in (m_t, α_s) as set out in Sect. 2.1 and Sect. 3.2 to the usual covariance matrix (which itself includes nuclear uncertainties and MHOU in addition to the experimental uncertainties), and then perform a global PDF fit using the usual NNPDF4.0 methodology [56] through the NNPDF framework [60]. We then simply determine the posterior distribution of (m_t, α_s) using the formulae set out in Sect. 2.1. If the shift from prior to posterior is particularly large, the fit can be repeated with a new prior, though in practice this is not usually necessary.

4.1 Closure test results

Fig. 4.1 displays the result of a closure test, performed at $\alpha_s^* = 0.118$ and $m_t^* = 172.5$ GeV at NNLO QCD accuracy, including MHOU's. In total, we analyse $N_{L_1} = 100$ replicas, each in turn consisting of $N_{L_2} = 100$ replicas, and show how their central values are distributed around the true values α_s^* and m_t^* . The corresponding weighted average and its covariance, Eqs. (2.25) and (2.26), are indicated by the (blue) ellipse, with the marginalised 68% confidence level (C.L.) intervals indicated by the (orange) shaded bands. We find compatibility between truth and the reconstructed values within 1σ , and thus conclude that our methodology is free from any significant bias. With only $N_{L_2} = 100$ replicas, we are confident that our methodological uncertainties are significantly less than one per mille in both α_s^* and m_t^* .

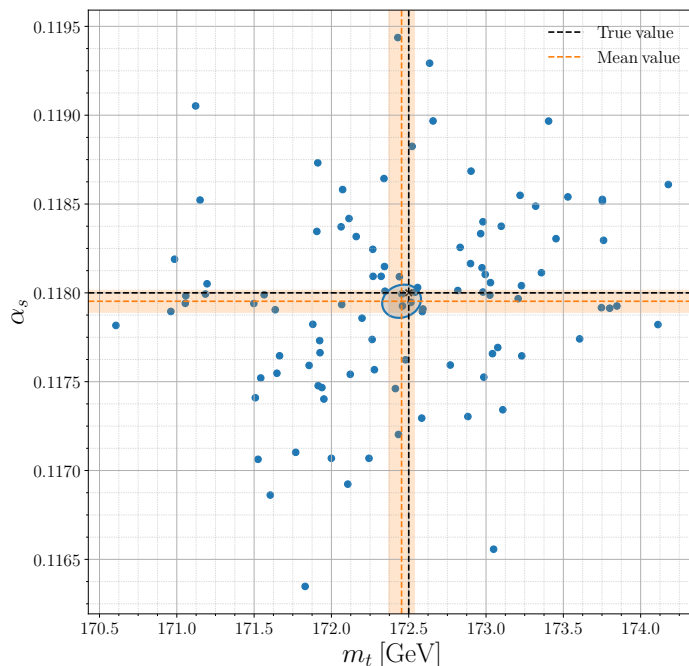


Figure 4.1: A closure test of $\alpha_s(m_Z)$ and m_t generated from 100 L_1 instances, each consisting of 100 L_2 replicas, at NNLO QCD while including MHOU's with underlying truth $\alpha_s^* = 0.118$ and $m_t^* = 172.5$ GeV. The weighted average of the L_1 instances, indicated by the (blue) ellipse, is compatible with the true values at 68% CL.

Although the closure test should pass regardless of the specific data sets included, we note for definiteness that the closure test shown in Fig. 4.1 includes all $t\bar{t}$ data sets differential in the top-quark pair rapidity $y_{t\bar{t}}$ as specified in Table 3.1. This is motivated by the fact that in our fits to real data, to be described in the next section, it is precisely this observable that is the least useful for determining m_t , producing results not always consistent with the more precise results given by some of the other observables. It is therefore interesting to see that even so, this observable still passes the closure test, despite these difficulties.

Near kinematic boundaries, where cross-sections are small, our assumption that data

are Gaussianly distributed may lead to a small fraction of negative replicas. In order to remedy this, the NNPDF4.0 determination imposed a constraint through the introduction of a Lagrange multiplier that penalised replicas giving negative cross-sections [56]. However, based on the fact that the TCM formalism assumes all data is Gaussian, we drop this constraint in the current work. However we continue to impose positivity on the PDFs themselves in the $\overline{\text{MS}}$ -scheme in the perturbative region [92]. This approach is slightly different to that adopted in the recent α_s determination in Ref. [50] where PDF positivity was also dropped in the closure test.

4.2 Determining m_t and $\alpha_s(m_Z)$ at NNLO

Having validated our methodology in Sect. 4.1 on pseudo data, we now move to applications to real data. Recalling that the various observables determined from the same data set are not independent, and that their inter-spectra correlations are not always (publicly) available, we study in the following the impact of each of the kinematic observables separately. In the few cases in which inter-spectra correlations are available, we comment on this explicitly and study their combined impact.

Observable	ATLAS	CMS	ATLAS + CMS
$(m_{t\bar{t}}, p_T^t)$	$m_t = 171.69 \pm 0.70$ $\alpha_s = 0.12093 \pm 0.00071$ $\rho = -0.086$		
$(m_{t\bar{t}}, y_{t\bar{t}})$	$m_t = 168.64 \pm 2.02$ $\alpha_s = 0.12059 \pm 0.00068$ $\rho = -0.073$	$m_t = 171.99 \pm 0.17$ $\alpha_s = 0.11924 \pm 0.00089$ $\rho = -0.324$	$m_t = 171.97 \pm 0.17$ $\alpha_s = 0.11918 \pm 0.00093$ $\rho = -0.329$
$m_{t\bar{t}}$	$m_t = 173.41 \pm 0.42$ $\alpha_s = 0.12085 \pm 0.00069$ $\rho = -0.017$	$m_t = 171.82 \pm 0.35$ $\alpha_s = 0.12047 \pm 0.00073$ $\rho = -0.068$	$m_t = 172.29 \pm 0.25$ $\alpha_s = 0.12050 \pm 0.00070$ $\rho = -0.100$
p_T^t	$m_t = 173.15 \pm 1.01$ $\alpha_s = 0.12084 \pm 0.00075$ $\rho = -0.000$	$m_t = 174.41 \pm 0.72$ $\alpha_s = 0.12066 \pm 0.00071$ $\rho = -0.026$	$m_t = 174.00 \pm 0.63$ $\alpha_s = 0.12061 \pm 0.00070$ $\rho = -0.032$
y_t	$m_t = 173.24 \pm 1.39$ $\alpha_s = 0.12070 \pm 0.00072$ $\rho = 0.080$	$m_t = 175.40 \pm 0.99$ $\alpha_s = 0.12065 \pm 0.00069$ $\rho = 0.050$	$m_t = 174.58 \pm 0.88$ $\alpha_s = 0.12054 \pm 0.00071$ $\rho = 0.089$
$y_{t\bar{t}}$	$m_t = 175.66 \pm 1.01$ $\alpha_s = 0.12066 \pm 0.00072$ $\rho = 0.146$	$m_t = 178.28 \pm 1.13$ $\alpha_s = 0.12045 \pm 0.00071$ $\rho = 0.119$	$m_t = 176.47 \pm 0.84$ $\alpha_s = 0.12017 \pm 0.00075$ $\rho = 0.173$

Table 4.1: The 68 % C.L. intervals on the top-quark mass, m_t , strong coupling constant, α_s , and their correlation coefficient, ρ , at NNLO with MHOU, for each of the observables plotted in Fig. 4.2, shown separately for ATLAS, CMS, and their combination (ATLAS+CMS).

Fig. 4.2 displays the 68% C.L. intervals at NNLO QCD accuracy in the (α_s, m_t) plane corresponding to fits carried out on our baseline data set, each supplemented with $t\bar{t}$ measurements differential in a variety of different kinematic observables. The numerical central values, uncertainties and correlation coefficients for the various ellipses are provided in Table 4.1. In total, we consider measurements differential either in the invariant mass $m_{t\bar{t}}$

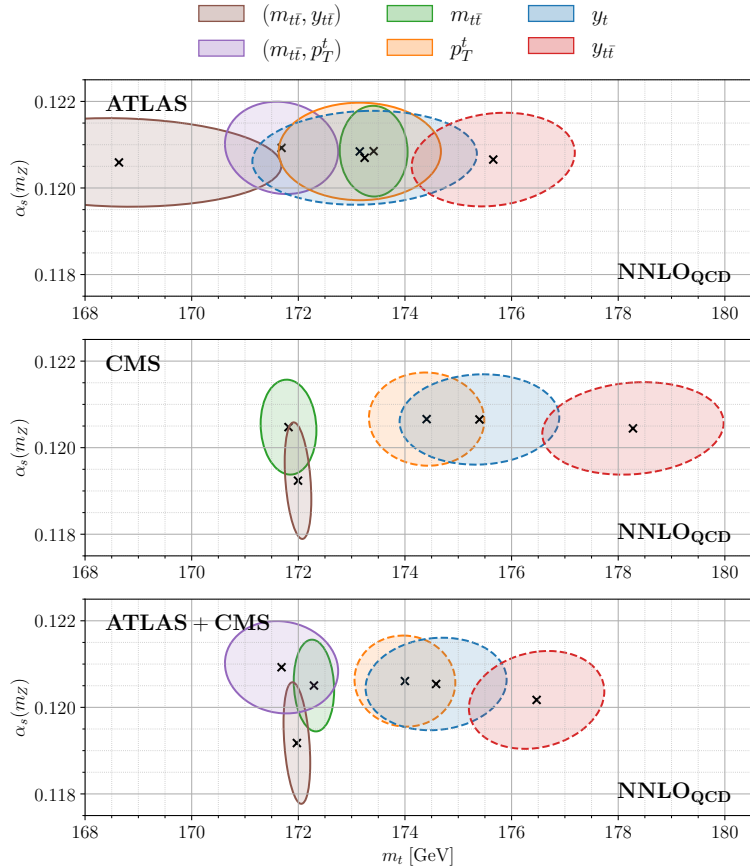


Figure 4.2: 68% C.L. bounds on the top-quark’s mass m_t and the strong couplings constant $\alpha_s(m_Z)$, at NNLO QCD with MHOU. In each case, multiple exclusion contours are shown, each corresponding to a fit performed on the baseline dataset complemented with top-quark data differential in the given observable. Each fit is done with 500 replicas. Ellipses with dashed lines indicate that at least one of the data sets in this measurement has a $\chi^2/n_{\text{dat}} > 3.0$

of the top-quark pair, the top-quark’s transverse momentum p_T^t , the top-quark’s rapidity y_t , the rapidity of the $t\bar{t}$ pair, $y_{t\bar{t}}$, and then also double differential distributions in either $(m_{t\bar{t}}, p_T^t)$ or $(m_{t\bar{t}}, y_{t\bar{t}})$. From top to bottom, we show first a determination based only on ATLAS $t\bar{t}$ measurements, followed by CMS $t\bar{t}$ measurements in the middle panel, and finally their combination in the bottom panel. All determinations share exactly the same data sets except for the relevant $t\bar{t}$ measurements. We refer to Table 4.2 for an overview of the $t\bar{t}$ data sets that enter each determination, together with their χ^2 normalised to the number of data points n_{dat} . In Fig. 4.2, ellipses with dashed lines indicate that at least one of the associated data sets has a $\chi^2/n_{\text{dat}} > 3.0$.

Several interesting observations can be made by inspecting Fig. 4.2 together with the χ^2 values in Table 4.2. First of all, we note a significant spread in m_t for the different ellipses, while α_s is instead relatively stable. This can be understood by noting that the data sets common to all the fits, in particular the DIS, Drell-Yan, single-jet and di-jet

Observable	Data set	n_{dat}	ATLAS			CMS			ATLAS+CMS		
			NNLO QCD	aN ³ LO QCD	aN ³ LO QCD ⊗ NLO _{QED}	NNLO QCD	aN ³ LO QCD	aN ³ LO QCD ⊗ NLO _{QED}	NNLO QCD	aN ³ LO QCD	aN ³ LO QCD ⊗ NLO _{QED}
$m_{t\bar{t}}$	ATLAS 13 TeV $t\bar{t}$ all hadr.	9	1.179	1.289	1.292				1.097	1.181	1.177
	ATLAS 13 TeV $t\bar{t} \ell + j$	9	0.944	0.954	0.895				0.928	0.917	0.857
	ATLAS 8 TeV $t\bar{t} 2\ell$	6	0.142	0.178	0.155				0.103	0.129	0.109
	ATLAS 8 TeV $t\bar{t} \ell + j$	7	0.228	0.179	0.202				0.295	0.235	0.261
	CMS 13 TeV $t\bar{t} 2\ell$ 138 fb ⁻¹	7				1.569	1.770	1.728	1.588	1.797	1.736
CMS 13 TeV $t\bar{t} \ell + j$	15				0.922	1.049	1.079	0.939	1.074	1.090	
total		53	0.854	0.856	0.847	1.199	1.300	1.302	1.167	1.191	1.185
$(m_{t\bar{t}}, p_T^t)$	ATLAS 13 TeV $t\bar{t} \ell + j$	15	0.516	0.471	0.436						
	total	15	0.516	0.471	0.436						
$(m_{t\bar{t}}, y_{t\bar{t}})$	ATLAS 13 TeV $t\bar{t}$ all hadr.	11	2.642	2.876	3.029				1.287	1.213	1.245
	CMS 13 TeV $t\bar{t} 2\ell$ 138 fb ⁻¹	16				1.947	1.899	1.920	1.902	1.826	1.850
	CMS 13 TeV $t\bar{t} \ell + j$	34				2.905	2.930	2.956	2.834	2.786	2.846
	total	61	2.642	2.876	3.029	2.708	2.714	2.741	2.419	2.365	2.416
	ATLAS 13 TeV $t\bar{t} \ell + j$	8	0.828	0.846	0.796				0.802	0.820	0.775
ATLAS 8 TeV $t\bar{t} \ell + j$	8	0.366	0.334	0.306				0.380	0.340	0.309	
CMS 13 TeV $t\bar{t} 2\ell$ 138 fb ⁻¹	7				3.080	3.276	3.231	3.050	3.258	3.235	
CMS 13 TeV $t\bar{t} \ell + j$	16				0.506	0.557	0.548	0.497	0.551	0.549	
total		39	0.554	0.551	0.519	1.408	1.467	1.449	1.053	1.087	1.077
y_t	ATLAS 13 TeV $t\bar{t} \ell + j$	5	0.686	0.676	0.715				0.695	0.675	0.714
	ATLAS 8 TeV $t\bar{t} \ell + j$	5	4.408	4.563	4.947				4.026	4.181	4.454
	CMS 13 TeV $t\bar{t} 2\ell$ 138 fb ⁻¹	10				3.170	3.146	3.123	3.169	3.130	3.110
	CMS 13 TeV $t\bar{t} \ell + j$	11				3.230	3.389	3.433	3.068	3.205	3.225
	total	31	2.670	2.745	2.967	3.123	3.197	3.208	2.877	2.913	2.951
$y_{t\bar{t}}$	ATLAS 13 TeV $t\bar{t}$ all hadr.	12	0.823	0.836	0.841				0.710	0.717	0.722
	ATLAS 13 TeV $t\bar{t} \ell + j$	7	0.695	0.742	0.766				0.402	0.422	0.429
	ATLAS 8 TeV $t\bar{t} 2\ell$	5	1.140	1.148	1.217				0.752	0.733	0.763
	ATLAS 8 TeV $t\bar{t} \ell + j$	5	3.986	3.949	4.189				2.526	2.407	2.625
	CMS 13 TeV $t\bar{t} 2\ell$	10				0.842	0.895	1.001	0.642	0.686	0.745
CMS 13 TeV $t\bar{t} \ell + j$	10				4.575	4.588	4.770	3.772	3.832	3.895	
total		49	1.334	1.337	1.395	2.930	2.971	3.138	1.586	1.596	1.650

Table 4.2: The χ^2/n_{dat} of each of the data sets entering the joint $\alpha_s(m_Z)$, m_t determinations split up according to whether only data sets from ATLAS, CMS or both are used as input to the fit. In each case, the χ^2 is given at NNLO QCD, aN³LO QCD, and aN³LO QCD with QED corrections. The corresponding bounds are provided in Table 4.4 and shown in Figs. 4.2 and 4.7. In all cases MHOU's are included.

measurements, are themselves all sensitive to α_s , while having no sensitivity to m_t . Thus α_s is mainly determined by these data sets, leaving the different top-quark data sets to determine m_t . An exception is the determination based on the $(m_{t\bar{t}}, y_{t\bar{t}})$ distribution from CMS, where we observe a rather lower value of $\alpha_s(m_Z)$. We traced this effect to a slight tension between this particular dataset and the single-jet and di-jet measurements. It is important to remark that the spread in central values of m_t from the different observables has nothing to do with the fitting methodology, since it disappears once considered in a closure test. Indeed, we refer to Fig. 4.1 for the equivalent result of the $y_{t\bar{t}}$ contour from Fig. 4.2 in the context of a closure test. It is interesting to note that the outlying observables tend to be those with relatively poor χ^2 . That the spread is somewhat broader in the case of CMS suggests the spread in m_t may in part be an experimental issue. At the same time, to the extent ATLAS and CMS display a similar pattern suggests that there may also be theoretical issues, perhaps in the theoretical description of other datasets in the fit such as jets [51].

Second, we observe a strong hierarchy in the precision with which each observable can be used to extract m_t , which is generally consistent between both ATLAS and CMS. The $(m_{t\bar{t}}, y_{t\bar{t}})$ double differential distributions from CMS in the dilepton and $\ell + j$ channels provide the most stringent bounds on m_t , and these dominate in the combination. The $(m_{t\bar{t}}, y_{t\bar{t}})$ distribution from ATLAS consists only of measurements in the fully hadronic channel which is plagued by large experimental and theoretical uncertainties, thus providing only a poor extraction of m_t . It is interesting that when this distribution is fitted together with the CMS measurements its χ^2 improves significantly, from 2.64 to 1.25. The single differential distributions in $m_{t\bar{t}}$, from both ATLAS and CMS, are all well fitted, and give rather precise results for m_t , as expected from the discussion in Fig. 3.1. The fact that the double differential distribution outperforms the single differential measurement matches the naive expectation that integrating over one of the observables incurs a loss of information, which in turn translates into a less precise m_t determination. The p_T^t distributions give somewhat less precise results for m_t , and one of them is rather poorly fitted.

The observables least sensitive to m_t are clearly the distributions in rapidities, either y_t or $y_{t\bar{t}}$. This we anticipated already, based on the kinematic distributions shown in Fig. 3.1, where varying m_t mainly changes the normalisation of the rapidity distribution rather than inducing any noticeable shape effects. Furthermore, besides its large uncertainty in m_t , the CMS $y_{t\bar{t}}$ distribution is a clear outlier compared to the other extractions. This can be explained by inspecting its χ^2 from Table 4.2 – the CMS 13 TeV measurement in the $\ell + j$ channel has a particularly high χ^2 of 4.58 (though again this improves in the combined fit). We have verified that, for this particular data set, the fitted predictions lie consistently above the experimental data, which the TCM corrects for by an increased value of m_t . Difficulties in fitting individual rapidity distributions have been previously encountered in Refs. [44, 56, 93].

Focusing now on the ATLAS+CMS combination, we note how precision improves with respect to considering either ATLAS or CMS separately, as expected for mutually consistent data. Moreover, results become increasingly more compatible when one restricts attention to determinations with a $\chi^2/n_{\text{dat}} < 3.0$, with the p_T^t , $(m_{t\bar{t}}, y_{t\bar{t}})$ and $m_{t\bar{t}}$ all now overlapping

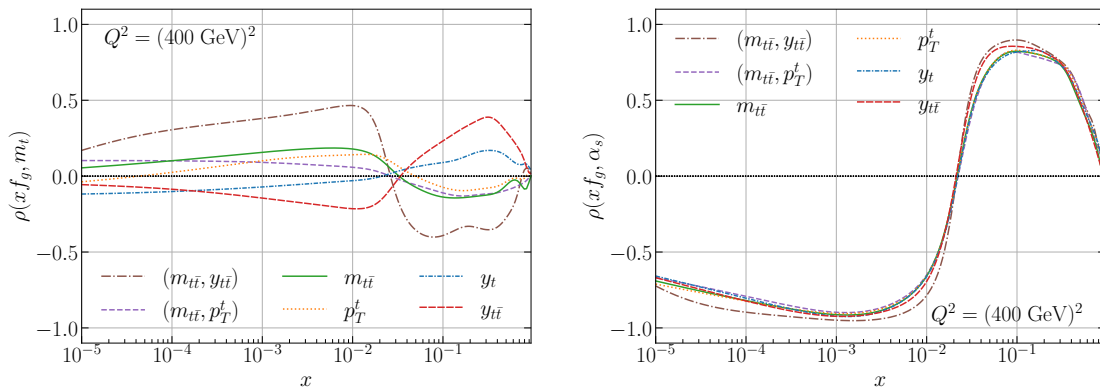


Figure 4.3: Left: The correlation $\rho(x f_g, m_t)$ between the gluon PDF f_g at NNLO QCD with MHOUs and the top-quark mass m_t as a function of Bjorken- x , for each of the observables in Fig. 4.2. Right: same, but for α_s instead of m_t .

within 1σ . The observable most sensitive to m_t with a satisfactory χ^2 of 1.17 is the single differential distribution in $m_{t\bar{t}}$, which in the ATLAS+CMS combination results in $m_t = 172.29 \pm 0.25$ GeV.

Regarding correlations between m_t and $\alpha_s(m_Z)$, we find that for $m_{t\bar{t}}$ and p_T^t they are consistently negative, while for rapidities they are consistently positive. This can be intuitively understood by noting that the rapidity is most sensitive to the gluon PDF which in turn affects $t\bar{t}$ production through the gluon fusion channel. This is consistent with Fig. 4.3, which displays the correlation pattern between the gluon PDF f_g and m_t (left panel), and between f_g and $\alpha_s(m_Z)$ (right panel), as a function of Bjorken- x for each of the observables considered in Fig. 4.2. We find that wherever the rapidities show positive correlations between m_t and the gluon PDF, they also show positive correlations with $\alpha_s(m_Z)$, while the opposite effect is instead observed for the other observables. The size of the correlations also reflects the degree of correlation between $\alpha_s(m_Z)$ and m_t . In the x -range relevant for $t\bar{t}$ production, the correlation of the gluon PDF with m_t is positive for $y_{t\bar{t}}$, less positive for y_t , but negative for $m_{t\bar{t}}$ and the joint distribution $(m_{t\bar{t}}, y_{t\bar{t}})$, consistent with the correlation pattern in Table 4.1.

Further inspecting the correlations in Fig. 4.3, we find that the gluon PDF is much more correlated to $\alpha_s(m_Z)$ than m_t , which is consistent with the fact that α_s enters in the evolution and hard cross-sections of all the data included in the fit, while m_t only enters the hard cross-sections of the top datasets. It follows that the correlation of the gluon with α_s is insensitive to the choice of top dataset, since it is predominantly due to the rest of the data in the global fit. While for $\alpha_s(m_Z)$ we find correlations of up to 0.75 in the mid to high- x region, for m_t the correlation is still as much 0.40, which is still significant. The change in sign of the correlation of α_s with the gluon (a consequence of the momentum sum rule) is reflected in a similar change of sign in the correlation of m_t with the gluon.

These results show that while the inclusion of correlations with the PDFs through the TCM (in what amounts to a joint fit) is essential for a global determination of α_s [50, 51],

it is also necessary for a reliable determination of the top mass m_t . The correlation of m_t with α_s is also significant, but rather less, and can be minimised by using the differential $m_{t\bar{t}}$ and p_T^t distributions. This gives us confidence that our best results for m_t are quite insensitive to the value of α_s , which is in agreement with the observations of Ref. [44], being determined rather by the shape of the top observables.

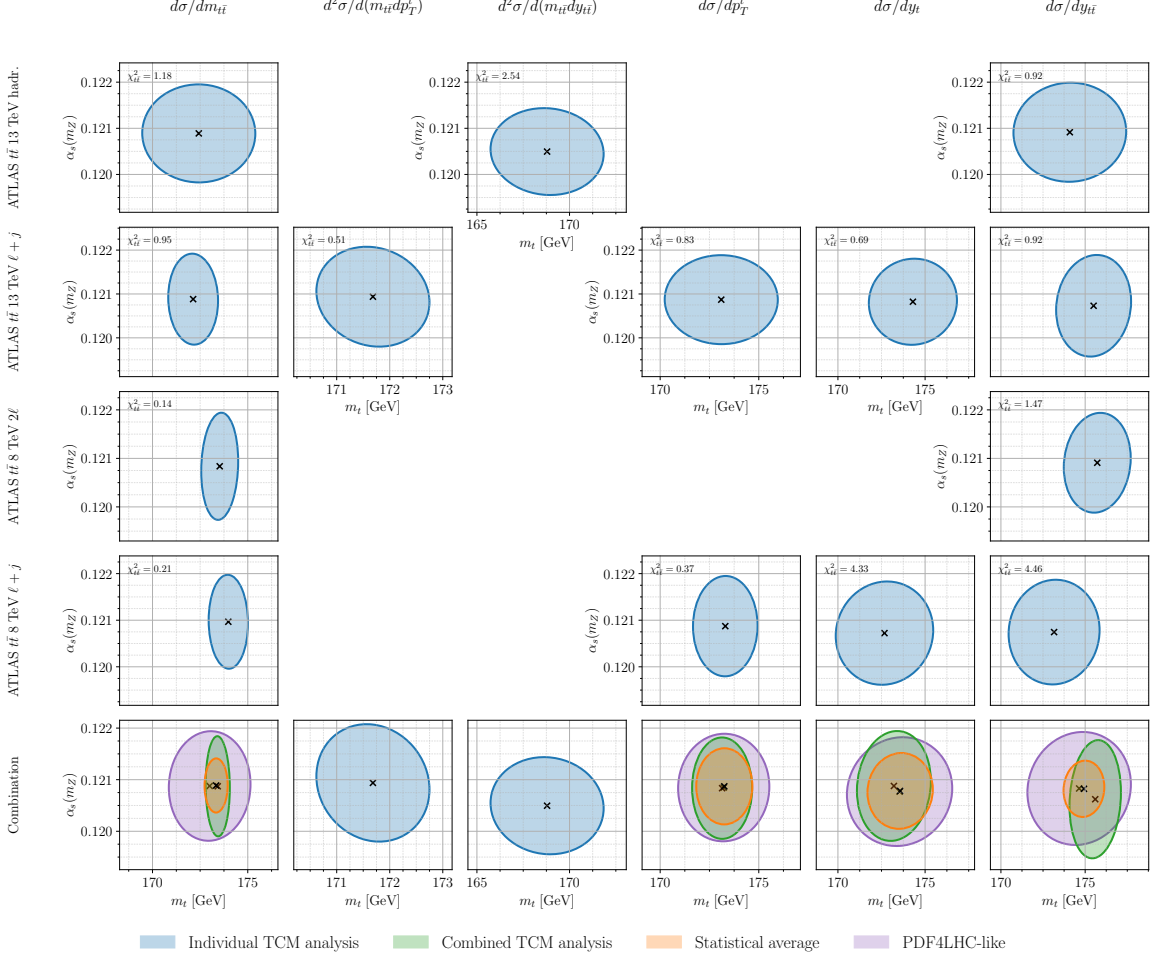


Figure 4.4: 68 % C.L. contours on the top-quark’s mass m_t and the strong coupling constant $\alpha_s(m_Z)$ at NNLO QCD with MHOU obtained from separate fits to top-quark data differential in distinct kinematic observables (columns) for various ATLAS data sets (rows), whenever available (all in blue). The bottom row shows the combination of all the datasets in the corresponding column, for each observable, made three different ways: the combined TCM analysis (in green), corresponding to a simultaneous fit including all data sets within each column, the statistical average of the individual TCM ellipses (in orange), and finally, the PDF4LHC-like combination obtained by combining all replicas with equal weights (in purple).

Statistical combinations An important question concerns how to statistically combine multiple measurements in order to faithfully account for all sources of uncertainties. This is a topic much discussed, both within the PDG, but also in the context of PDFs (see, for

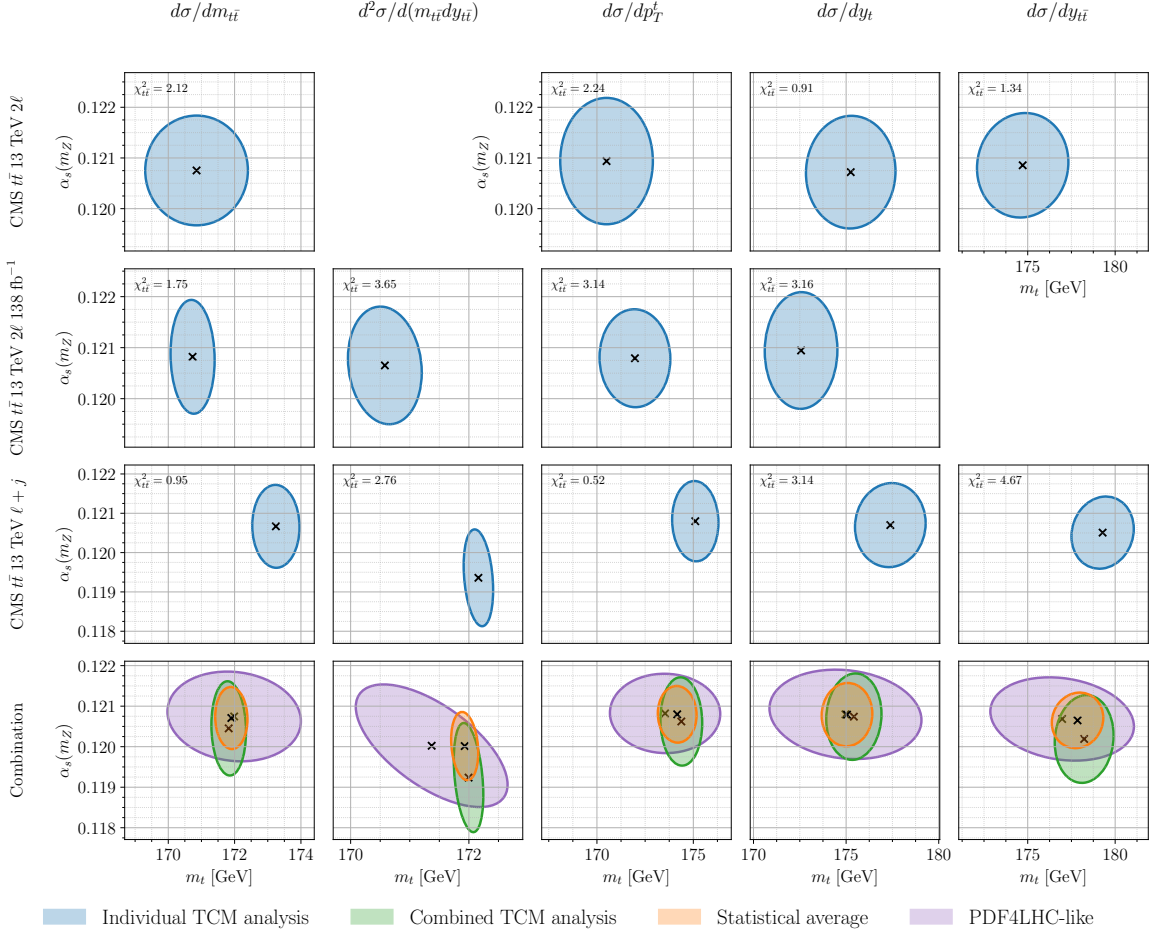


Figure 4.5: Same as Fig. 4.4, now for the CMS datasets.

example, Ref. [94] and references therein). To this end, we show in Figs. 4.4 and 4.5 the breakdown of the individual measurements that enter Fig. 4.2 in the case of ATLAS and CMS, respectively. In each column, we display results for a single kinematic observable, while the rows distinguish between the various data sets. Whenever a given data set does not provide measurements differential in the given observable, a blank entry is shown. In the bottom row, we display the combination of all the data sets in the corresponding column, for each observable, made in three different ways. First we show the combined TCM analysis, which corresponds to what is shown in Fig. 4.2. Its result is obtained from a single fit including all data sets in this column. Second, we show the statistical average, which does not correspond to a new fit, but rather to an a posteriori combination of the previous ellipses weighted according to their means and covariances following Eqs. 2.25 and 2.26. The third way of combining determinations is labelled “PDF4LHC-like”, which corresponds to instead an unweighted average where all replicas that make up the individual TCM analyses are used collectively to determine a new exclusion contour [95].

A clear pattern arises from the combinations in Fig. 4.4 and Fig. 4.5. As expected, the “PDF4LHC-like” combination is the most conservative, significantly overestimating

uncertainties, (though always including the correct central value within this uncertainty). This is because it treats all the datasets with equal weight, irrespective of their precision or consistency. An envelope prescription would give even broader uncertainties. The statistical average, by contrast, assumes that the determinations made with each top dataset are uncorrelated, ignoring the fact that apart from the top data, the underlying dataset used to determine the PDFs is the same in each. It thus underestimates uncertainties, especially in α_s . In effect such a combination essentially reuses the same data multiple times. Since we have considerably more data to constrain α_s , such as all DIS, single-jet and di-jet data, than we have for m_t , the effect is much more visible there. However it is also visible in the m_t determination, particularly for the rapidity distributions where the correlation with the PDFs is stronger. The correct combination is provided by the combined TCM analysis, which takes into account properly all correlations between the data sets due to the PDFs, α_s and m_t , with no double counting.

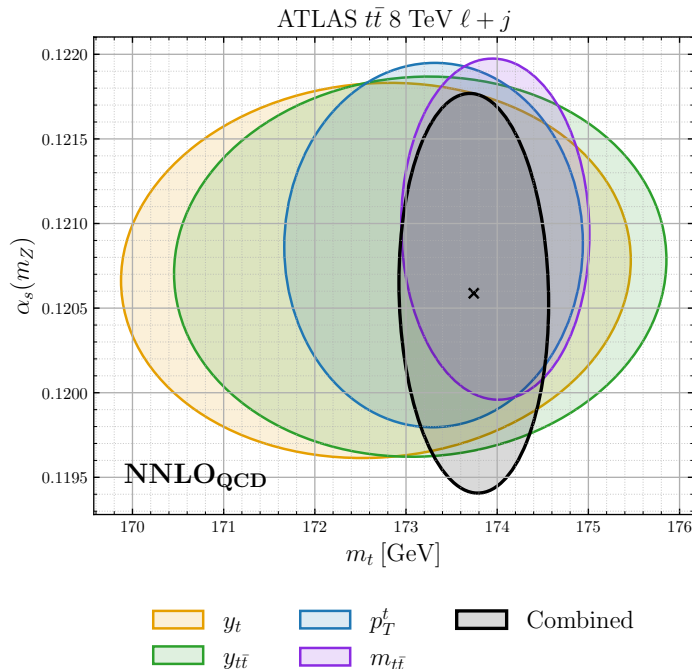


Figure 4.6: The 68% C.L. contours in the (α_s, m_t) plane comparing the impact of analysing each of the observables y_t , $y_{t\bar{t}}$, p_T^t , $m_{t\bar{t}}$ entering the ATLAS $t\bar{t}$ 8 TeV $\ell + j$ data set individually versus their combined impact when considering their inter-spectra correlations.

Inter-spectra correlations In the case of the ATLAS $t\bar{t}$ 8 TeV measurement in the $\ell + j$ channel, inter-spectra correlations are known. This means that all observables within this data set may be analysed simultaneously. We display in Fig. 4.6 a comparison between the constraints at the 68% C.L. obtained either when analysing one observable at the time versus the combination that considers y_t , $y_{t\bar{t}}$, p_T^t and $m_{t\bar{t}}$ simultaneously, and provide the corresponding χ^2 values in Table 4.3. It is clear how the combination provides more stringent constraints on m_t than any of the observables individually. Inspecting the χ^2

χ^2/n_{dat}	Individual spectra	Combined
$m_{t\bar{t}}$	0.21	0.30
p_T^t	0.37	0.40
y_t	4.33	3.58
$y_{t\bar{t}}$	4.46	3.81
Total	–	1.86

Table 4.3: The χ^2/n_{dat} corresponding to Fig. 4.6 for the ATLAS 8 TeV $\ell + j t\bar{t}$ differential spectra, shown for each distribution when fitted individually and in the combined analysis where inter-spectra correlations are considered.

values in Table 4.3, we find that the χ^2 of each of the individual spectra improves when considered as part of the combined fit, an effect that can partially be attributed to the fact that the $t\bar{t}$ data now receive a relatively larger weight with respect to the other processes in the fit. This provides a clear motivation for publishing information on the inter-spectra correlations, and we hope in the future these will also be provided for some of the other data sets.

Note in this context that while for the ATLAS $t\bar{t}$ 13 TeV measurement in the $\ell + j$ channel we have the covariance matrix for each spectrum, including both statistical and systematic uncertainties, and the inter-spectra statistical correlations, we don't have the correlations of systematics across spectra in the form of an off-diagonal covariance matrix. These elements can in principle be inferred by assuming that contributions from the same source are fully correlated, and that the asymmetric uncertainties are symmetrized using a particular prescription. Pending clarification on both these issues, we postpone an examination of the inter-spectra correlations in this data set for future work.

4.3 Impact of other small corrections

With our baseline results established at NNLO with MHOU, and the demonstration that the current cross-sections are actually sufficient to determine the top mass to a precision of a few tenths of a GeV, we now move to study the impact of various small cumulative corrections. First, we consider aN³LO QCD corrections, followed by the addition of mixed QCD \otimes QED corrections and the photon PDF. On top of this, we then consider EW corrections to the $t\bar{t}$ matrix element, the toponium correction, and finally the impact of the FLAG determination of α_s .

aN³LO corrections The left panel of Fig. 4.7 shows the impact of aN³LO QCD evolution effects in the (α_s, m_t) plane. The corresponding numerical bounds on m_t are collected in Table 4.4. Comparing these against the NNLO results in that same table, we observe how aN³LO perturbative corrections push the top mass down for nearly all observables, with m_t moving down by around 0.3 GeV in the case of $m_{t\bar{t}}$, while rapidity based extractions push m_t down almost by 1 GeV. This effect we have narrowed down to a decreased gluon luminosity at aN³LO around the $t\bar{t}$ threshold, which the fit compensates by preferring a

higher partonic cross-section, which in turn is realised at lower values of the top mass. We do not observe any significant shift in α_s , which confirms that our MHOUs at NNLO QCD correctly account for higher order effects. This was previously also observed in Ref. [50]. Regarding the fit quality, from Table 4.2 we can conclude that the χ^2 to the top datasets is little changed on going from NNLO to aN³LO QCD, as we would expect given that in both cases the top cross-section is evaluated at NNLO with an estimate for MHOUs.

Beyond NNLO QCD, one may also ask about the impact of soft gluon resummation effects on our m_t determination. In the case of the CMS dilepton measurement at 13 TeV from Ref. [7], NNLL' corrections have been computed in Ref. [96], and we have verified explicitly that these lead to no noticeable change in our m_t determination, confirming that our MHOUs already capture these higher order effects. We therefore do not consider any soft gluon resummation effects in this work. However, if NNLL' corrections become available for the other datasets, it could be interesting to revisit their (combined) impact.

It would also be interesting in the future to attempt to construct an approximation to the N³LO differential top cross-sections by combining the results from soft gluon resummation with those from high energy resummation [97–99], along the lines of the aN³LO result already obtained for the total cross-section [100]. Such an approximation might potentially increase the precision and accuracy of our top mass determination.

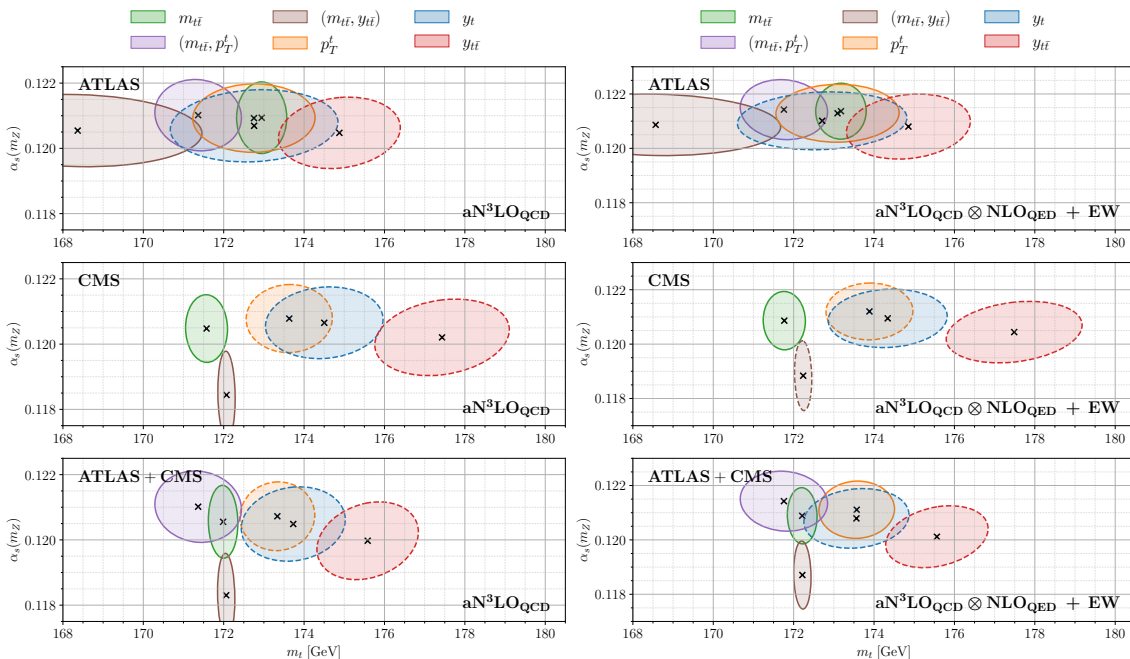


Figure 4.7: Left: same as Fig. 4.2, now at aN³LO QCD accuracy. Right: same, now at aN³LO QCD accuracy including mixed QCD⊗QED PDF evolution, as well as EW corrections at the level of the $t\bar{t}$ matrix element.

QED evolution and EW corrections We now move to study the impact on the top mass of, first, joint QCD⊗QED evolution and the photon PDF, followed by the impact of additionally including EW corrections in the hard $t\bar{t}$ matrix element.

	m_t [GeV]	m_t [GeV]	m_t [GeV]
Observable	NNLO_{QCD}	aN³LO_{QCD}	aN³LO_{QCD} \otimes NLO_{QED}
$m_{t\bar{t}}$	172.29 ± 0.25	171.99 ± 0.24	171.95 ± 0.25
p_T^t	174.00 ± 0.63	173.34 ± 0.62	173.24 ± 0.62
y_t	174.58 ± 0.88	173.73 ± 0.86	173.62 ± 0.86
$y_{t\bar{t}}$	176.47 ± 0.84	175.58 ± 0.84	175.51 ± 0.84
$(m_{t\bar{t}}, p_T^t)$	171.69 ± 0.70	171.36 ± 0.71	171.39 ± 0.72
$(m_{t\bar{t}}, y_{t\bar{t}})$	171.97 ± 0.17	172.06 ± 0.14	172.00 ± 0.14
	aN³LO_{QCD} \otimes NLO_{QED} + EW	aN³LO_{QCD} \otimes NLO_{QED} + EW + topo.	aN³LO_{QCD} \otimes NLO_{QED} + EW + topo. + FLAG
$m_{t\bar{t}}$	172.21 ± 0.24	172.80 ± 0.26	172.82 ± 0.27
p_T^t	173.57 ± 0.62	173.76 ± 0.64	173.77 ± 0.66
y_t	173.56 ± 0.87	173.70 ± 0.86	173.65 ± 0.88
$y_{t\bar{t}}$	175.56 ± 0.84	175.67 ± 0.85	175.71 ± 0.87
$(m_{t\bar{t}}, p_T^t)$	171.76 ± 0.72	171.98 ± 0.72	172.02 ± 0.74
$(m_{t\bar{t}}, y_{t\bar{t}})$	172.22 ± 0.14	172.95 ± 0.24	172.97 ± 0.25

Table 4.4: Overview of the 68% C.L. bounds on the top-quark pole mass, m_t , for each of the observables and theory settings considered in this work. The upper half consists of, first, our baseline NNLO QCD theory, followed by the addition of aN³LO QCD corrections to the PDF evolution, and mixed QCD \otimes QED evolution. The lower half then additionally includes, first, EW corrections to the $t\bar{t}$ matrix element, a toponium correction, and finally the FLAG constraint imposed as prior on $\alpha_s(m_Z)$.

Considering first the impact of QED evolution corrections, we provide in the top-right column of Table 4.4 the corresponding bounds on m_t . With respect to the aN³LO result we observe only minor differences, which is expected given that the $t\bar{t}$ hard matrix element in this particular fit is evaluated at NNLO QCD accuracy without any EW corrections in the $t\bar{t}$ hard matrix element. Let us therefore analyse now explicitly the impact of EW corrections as discussed in Sect. 3.2. The corresponding bounds are provided in the bottom-left column of Table 4.4. Compared to the equivalent setup without EW corrections (top-right column), we note how the EW corrections push m_t up by around 0.3 GeV in the case of $m_{t\bar{t}}$ and p_T^t based distributions, while little effect is seen in the case of rapidity based distributions. This is consistent with the relative size of the EW corrections. Indeed, recalling Fig. 3.2, we observe how EW corrections modify the $m_{t\bar{t}}$ and p_T^t distributions at the percent level, while only per-mille level effects are observed in the case of rapidity distributions.

In the leftmost results column labeled “+EW” in Table 4.5, we present the χ^2 values while including EW corrections for the ATLAS and CMS combination. As compared to the same setup without EW corrections, see Table 4.2, we find that including EW corrections improves the fit quality of the $m_{t\bar{t}}$ and p_T^t distributions, reducing the χ^2 from 1.185 to 1.156 and from 1.077 to 1.063, respectively. A slight deterioration is observed instead in

the case of the rapidity distributions, which could possibly be explained by an increased tension with the jet data [50].

Regarding their combined impact on $\alpha_s(m_Z)$, after comparing the left and right panels in Fig. 4.7 we find that QED evolution and EW corrections lead to an increase of $\alpha_s(m_Z)$ by a few per-mille. This is similar to the effect that was also observed in Ref. [50], which was explained by noting how the photon PDF subtracts momentum from the gluon PDF which in turn is compensated by a slightly higher value of α_s .

Observable	Data set	n_{dat}	aN ³ LO _{QCD} ⊗NLO _{QED}		
			+ EW	+ EW + toponium	+ EW + toponium + FLAG
$m_{t\bar{t}}$	ATLAS 13 TeV $t\bar{t}$ all hadr.	9	1.096	1.103	1.117
	ATLAS 13 TeV $t\bar{t} \ell + j$	9	0.802	0.843	0.785
	ATLAS 8 TeV $t\bar{t} 2\ell$	6	0.078	0.068	0.050
	ATLAS 8 TeV $t\bar{t} \ell + j$	7	0.319	0.372	0.446
	CMS 13 TeV $t\bar{t} 2\ell$ 138 fb ⁻¹	7	1.532	1.379	1.466
	CMS 13 TeV $t\bar{t} \ell + j$	15	0.974	0.963	1.162
	total	53	1.156	1.079	1.094
$(m_{t\bar{t}}, p_T^t)$	ATLAS 13 TeV $t\bar{t} \ell + j$	15	0.480	0.516	0.511
	total	15	0.480	0.516	0.511
$(m_{t\bar{t}}, y_{t\bar{t}})$	ATLAS 13 TeV $t\bar{t}$ all hadr.	11	1.194	1.202	1.278
	CMS 13 TeV $t\bar{t} 2\ell$ 138 fb ⁻¹	16	1.881	1.883	1.845
	CMS 13 TeV $t\bar{t} \ell + j$	34	2.901	2.887	2.952
	total	61	2.450	2.450	2.479
p_T^t	ATLAS 13 TeV $t\bar{t} \ell + j$	8	0.764	1.171	1.094
	ATLAS 8 TeV $t\bar{t} \ell + j$	8	0.422	0.574	0.530
	CMS 13 TeV $t\bar{t} 2\ell$ 138 fb ⁻¹	7	2.985	2.745	2.690
	CMS 13 TeV $t\bar{t} \ell + j$	16	0.511	0.671	0.643
	total	39	1.063	1.166	1.133
y_t	ATLAS 13 TeV $t\bar{t} \ell + j$	5	0.718	0.705	0.764
	ATLAS 8 TeV $t\bar{t} \ell + j$	5	4.741	4.564	4.725
	CMS 13 TeV $t\bar{t} 2\ell$ 138 fb ⁻¹	10	3.100	3.103	3.063
	CMS 13 TeV $t\bar{t} \ell + j$	11	3.341	3.334	3.241
	total	31	3.016	2.994	2.974
$y_{t\bar{t}}$	ATLAS 13 TeV $t\bar{t}$ all hadr.	12	0.737	0.740	0.739
	ATLAS 13 TeV $t\bar{t} \ell + j$	7	0.460	0.471	0.474
	ATLAS 8 TeV $t\bar{t} 2\ell$	5	0.799	0.781	0.811
	ATLAS 8 TeV $t\bar{t} \ell + j$	5	2.761	2.641	2.796
	CMS 13 TeV $t\bar{t} 2\ell$	10	0.825	0.806	0.869
	CMS 13 TeV $t\bar{t} \ell + j$	10	4.129	4.094	3.983
	total	49	1.741	1.715	1.718

Table 4.5: The χ^2/n_{dat} values corresponding to the combined fits to ATLAS and CMS data at aN³LO_{QCD}⊗NLO_{QED} supplemented successively by EW and toponium corrections, and finally the FLAG prior on $\alpha_s(m_Z)$.

Toponium corrections To assess quantitatively the impact of toponium corrections we display in the left panel of Fig. 4.8 the 68% C.L. bounds in the presence of toponium corrections when added on top of the aN³LO_{QCD} ⊗ NLO_{QED} theory with EW corrections.

The numerical bounds are provided in Table 4.4 (lower half, second column). As discussed in Sect. 3.3, this includes a 50% theoretical uncertainty on the total toponium cross-section.

Compared to the equivalent setup without toponium corrections (lower half, first column), we observe that toponium generally moves m_t up by about 0.6 GeV in the case of the single differential distributions in $m_{t\bar{t}}$, corresponding to about 1.7σ , while m_t receives an upward shift of 0.7 GeV in the case of the the double differential distribution in $(m_{t\bar{t}}, y_{t\bar{t}})$, corresponding to about 2.7σ . We also note how the uncertainty on m_t generally increases when toponium corrections are included, as expected, since the toponium theory covariance matrix in Eq. (3.7) gives m_t greater freedom to move up and down in the bins around the $t\bar{t}$ threshold. By contrast, toponium corrections have no significant impact in determinations based on the rapidity distributions y_t and $y_{t\bar{t}}$. This is in line with the fact that the toponium signal appears localised around threshold in the $m_{t\bar{t}}$ distributions, while it contributes more uniformly across the rapidity bins, thereby washing out its effect. In all cases, the uncertainties do not change appreciably. As a result of this upward shift, the overall compatibility across the different observables improves. With the exception of the $y_{t\bar{t}}$ based determination, all observables now lead to values of m_t whose one sigma uncertainties all overlap.

Regarding the fit quality, from inspecting Table 4.5 we observe that the χ^2 generally improves under the addition of toponium with the exception of the p_T^t based determination, which suggest that overall the $t\bar{t}$ data sets prefer the addition of a toponium correction.

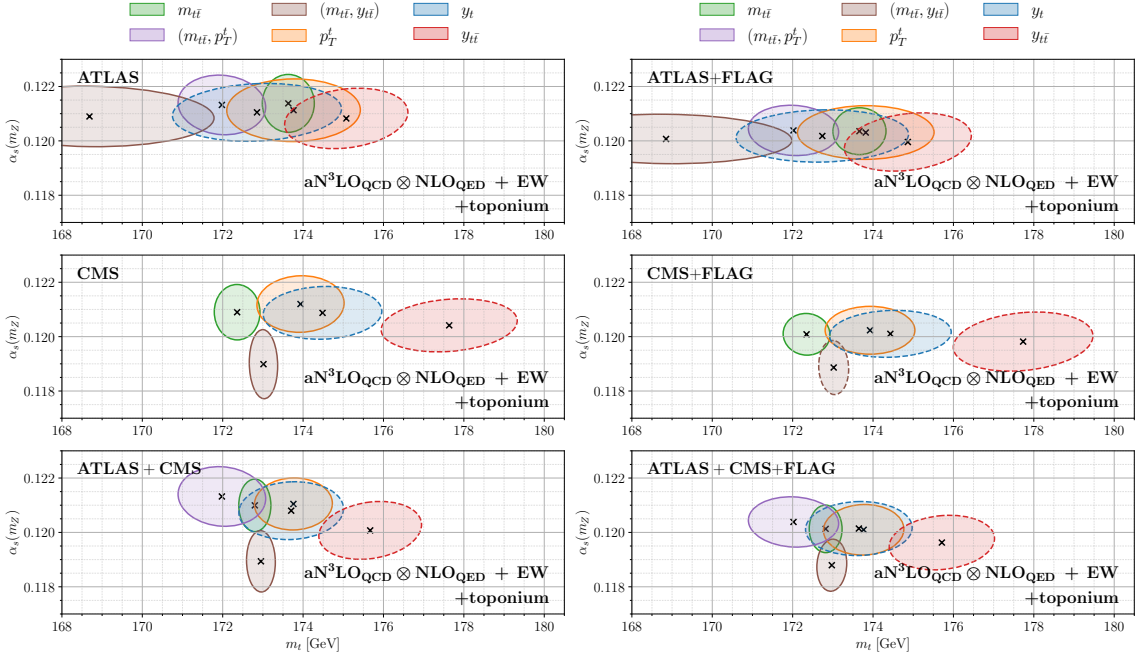


Figure 4.8: Left: same as the right panel of Fig. 4.7, now in the presence of toponium corrections. Right: same, except we now set the $\alpha_s(m_Z)$ prior to the FLAG24 constraints [91].

FLAG determination of α_s The recent lattice combination from FLAG [91, 101–110] provides a stringent bound on $\alpha_s(m_Z)$, namely $\alpha_s(m_Z) = 0.1183 \pm 0.0007$. In light of the fact that this is considerably lower than most of our α_s determinations, it is interesting to analyse to what extent this might affect our m_t determination.

Our starting point is the observation that the lattice result relies on input data independent of any data included in our PDF fits, meaning that it can be safely incorporated into our fit without double counting. To this end, we impose a prior on $\alpha_s(m_Z)$ around $\alpha_s(m_Z) = 0.1183 \pm 0.0007$ and generate theoretical predictions at $\alpha_s(m_Z) = \{0.1176, 0.1183, 0.1190\}$ in order to construct the corresponding theory covariance matrix as discussed in Sect. 2.1. We then repeat our analysis at $\text{aN}^3\text{LO}_{\text{QCD}} \otimes \text{NLO}_{\text{QED}}$ with EW corrections and toponium. The result is displayed in the right panel of Fig. 4.8. We can clearly see how $\alpha_s(m_Z)$ now comes out considerably lower, although the experimental data in the PDF fit still prefer a value of $\alpha_s(m_Z)$ higher than FLAG by about 1.5σ . Importantly, inspecting Table 4.4, we see no significant shifts in our m_t determinations, as expected given the relatively weak correlation of m_t with α_s . The same holds for the χ^2 values, as is clear from the rightmost column in Table 4.5.

4.4 Comparison to other determinations of the top mass

Finally, we comment, whenever possible, on how our results compare with some previous determinations. In particular, we compare with cross-section based measurements and direct reconstruction measurements from ATLAS and CMS, the ABMPtt determination [47], the MSHT determination [44], and the analysis of Ref. [43] that adopts a fixed PDF set.

ATLAS and CMS Fig. 4.9 shows a comparison of our determination of m_t with those reported by ATLAS and CMS. Results are grouped into indirect measurements (upper panel), which are based on similar measurements of $t\bar{t}$ production cross-sections to those used in our own determination, and direct measurements (middle panel), which are based instead on reconstruction of the top mass from measurements of the kinematics of the final state after the top quarks decay. While the direct measurements are significantly more precise, they rely rather heavily on Monte Carlo event generators, and thus suffer from a potential ambiguity in the precise definition of the top mass.

In the lower panel, we indicate the global determinations we obtained in the current work, using the various theoretical variations that we considered. We have restricted this to invariant mass based determinations given that these show the best compromise between precision and goodness of fit. Inspecting Fig. 4.9, it is remarkable that our indirect cross-section based measurement is very consistent with the direct measurements, and even a little bit more precise. This can be explained by noting that our fit combines multiple ATLAS and CMS measurements from different data sets while simultaneously taking account of correlations through the PDFs and α_s .

ABMPtt Next, we compare our results at NNLO QCD with MHOUs to the simultaneous ABMPtt determination from Ref. [47] (see in particular Table I therein). Our analysis differs in many respects from that used by ABMPtt: they also fit the PDFs together with m_t and α_s , but using a fixed functional form; their treatment of heavy quarks is different,

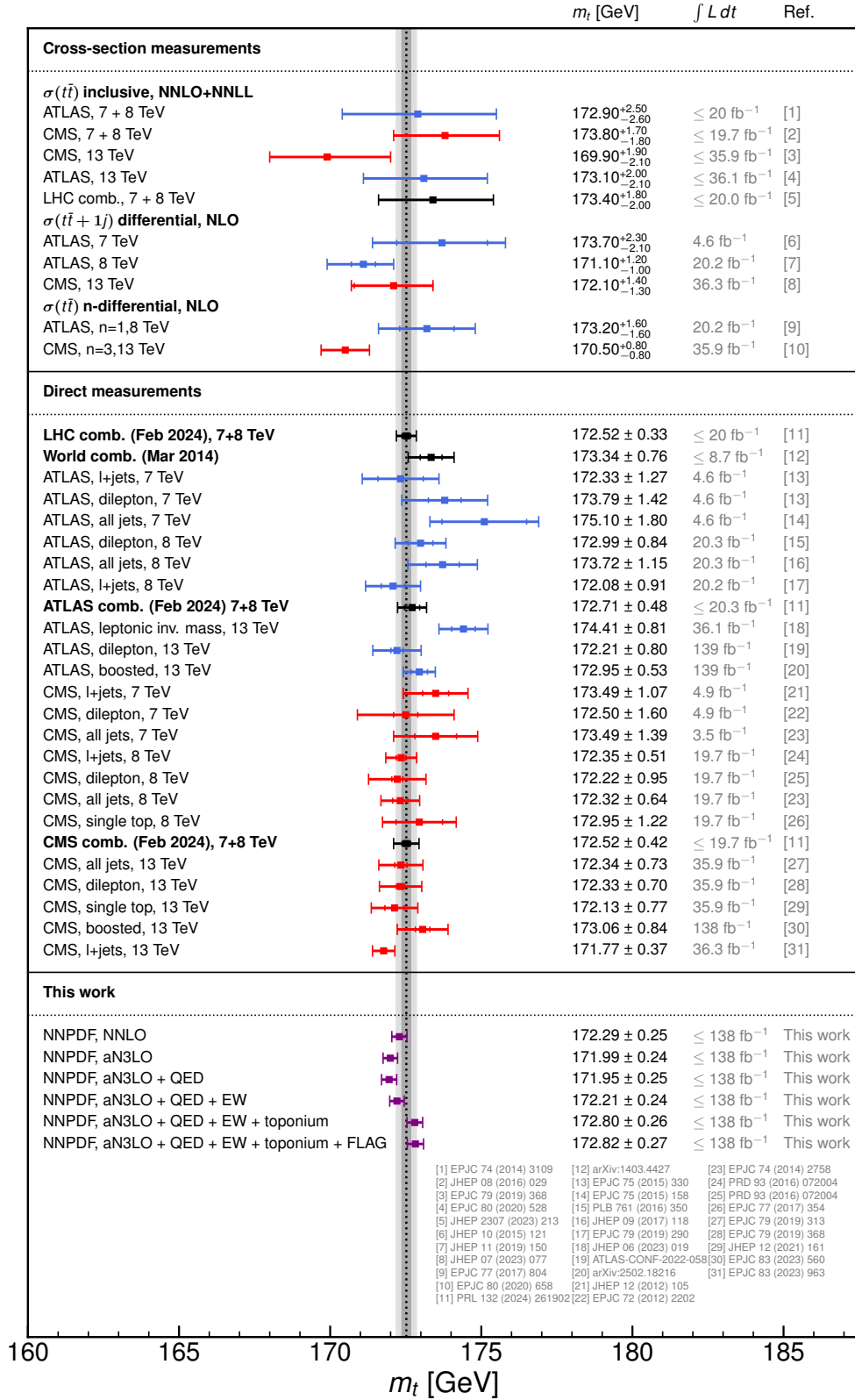


Figure 4.9: A comparison between cross-section based measurements and direct reconstruction measurements by ATLAS and CMS versus our determination based on cross-section measurements differential in the invariant mass of the top-quark pair. The grey band denotes the LHC combination from Feb 2024, which combines 7 and 8 TeV data from ATLAS and CMS. The plot is adapted from the LHCTopWG top mass summary plots, May 2025.

and they do not account for MHOU's. Moreover no jet data is included in the ABMPtt determination, which is especially relevant given the fact that this together with the top data is largely what determines the gluon PDF [50, 51]. Finally Ref. [47] determines the $\overline{\text{MS}}$ mass $m_t^{\overline{\text{MS}}}$ rather than the pole mass: we convert $m_t^{\overline{\text{MS}}}$ to the pole mass at four loops in QCD in order to make a numerical comparison (see Ref. [17] and in particular Eq. (61.1) therein).

We include in Table 4.6 a comparison of the top data sets that enter both analyses. For the purpose of this comparison, we have rerun our analysis using normalised differential $t\bar{t}$ distributions rather than absolute ones. Comparing first the ATLAS 13 TeV fully hadronic double differential measurement in $(m_{t\bar{t}}, y_{t\bar{t}})$, we find a compatible value for m_t within uncertainties, with a comparable size of the uncertainty itself. However using the CMS 13 TeV measurement in the $\ell + j$ channel we find a value of m_t around 4σ higher than the one from ABMPtt, with an uncertainty that is more than five times smaller. The precise reason for this substantial discrepancy is unclear.

MSHT Ref. [44] presented a simultaneous determination of the top-quark pole mass m_t , $\alpha_s(m_Z)$, and the PDFs within the global MSHT PDF framework. They also use a given PDF parametrization, and have no MHOU's, but they do include inclusive jet data to constrain the gluon. Their analysis focusses on top-quark data in the $\ell + j$ channel at 8 TeV from ATLAS and CMS, each differential in $m_{t\bar{t}}$, p_T^t and the rapidities y_t and $y_{t\bar{t}}$. No other channels were considered. In the case of ATLAS, they include all observables simultaneously while accounting for inter-spectra correlations through a specific decorrelation model [111]. In the case of CMS, they fit one observable at a time, since no inter-spectra correlations are available for this data set. The corresponding theoretical predictions are obtained with NNLO QCD supplemented with EW corrections. In line with our analysis, they observe only a very weak correlation between m_t and $\alpha_s(m_Z)$. After an initial simultaneous fit, they exploit this weak correlation to perform m_t determinations at a fixed value of $\alpha_s(m_Z) = 0.118$. We show in Table 4.6 the bounds on m_t obtained by MSHT from a fit to the ATLAS 8 TeV data set in the $\ell + j$ channel single differential in p_T^t , $m_{t\bar{t}}$, $y_{t\bar{t}}$ and y_t while considering inter-spectra correlations at $\alpha_s = 0.118$. This is consistent with our determination displayed in Fig. 4.6 within one standard deviation, and with a comparable size of the uncertainty. The final result reported by MSHT, including also CMS differential data, is $m_t = 173.0 \pm 0.6$ GeV, fully compatible with our determination of $m_t = 172.80 \pm 0.26$ GeV.

Fixed PDF determinations Finally, we can also compare our results against determinations using fixed PDFs [43], shown in the last two rows of Table 4.6. These analyse the ATLAS data taken at 8 TeV in the $\ell + j$ channel, using NNPDF3.1 [112] for the PDFs, but performing a combined fit to m_t and α_s . Note that this approach neglects correlations with the PDFs, so we do not expect to find agreement a priori. Using the single differential p_T^t observable they find a result for m_t a little higher than our own, but roughly compatible within uncertainties. Using the observable differential in $m_{t\bar{t}}$, we find statistically compatible results for m_t , while $\alpha_s(m_Z)$ comes out significantly lower in Ref. [43]. This

	Other determinations	This work
Data set and observable	ABMPtt [47]	
ATLAS 13 TeV $t\bar{t}$ all hadr. $1/\sigma d\sigma/d(m_{t\bar{t}}, y_{t\bar{t}})$	$m_t^{\overline{\text{MS}}} = 160.5 \pm 2.0$ GeV $m_t^{\text{pole}} = 169.98 \pm 2.1$ GeV	$m_t^{\text{pole}} = 166.49 \pm 1.91$ GeV $\alpha_s = 0.12082 \pm 0.00069$
CMS 13 TeV $t\bar{t} \ell + j$ $1/\sigma d\sigma/d(m_{t\bar{t}}, y_{t\bar{t}})$	$m_t^{\overline{\text{MS}}} = 158.7 \pm 0.9$ GeV $m_t^{\text{pole}} = 168.09 \pm 1.0$ GeV	$m_t^{\text{pole}} = 171.70 \pm 0.14$ GeV $\alpha_s = 0.11906 \pm 0.00064$
	MSHT [44]	
ATLAS 8 TeV $t\bar{t} \ell + j$ $d\sigma/dp_T^t, d\sigma/dm_{t\bar{t}}, d\sigma/dy_{t\bar{t}}, d\sigma/dy_t$	$m_t^{\text{pole}} = 172.4$ GeV < $m_t < 173.6$ GeV $\alpha_s = 0.118$ (fixed)	$m_t^{\text{pole}} = 173.74 \pm 0.54$ GeV $\alpha_s = 0.12059 \pm 0.00071$
	Ref. [43]	
ATLAS 8 TeV $t\bar{t} \ell + j$ $d\sigma/dp_T^t$	$m_t^{\text{pole}} = 175.6^{+1.0}_{-1.0}$ GeV $\alpha_s = 0.1210^{+0.0024}_{-0.0023}$	$m_t^{\text{pole}} = 173.30 \pm 1.08$ GeV $\alpha_s = 0.12059 \pm 0.00078$
ATLAS 8 TeV $t\bar{t} \ell + j$ $d\sigma/dm_{t\bar{t}}$	$m_t^{\text{pole}} = 173.5^{+0.5}_{-0.5}$ GeV $\alpha_s = 0.1176^{+0.0022}_{-0.0022}$	$m_t^{\text{pole}} = 173.98 \pm 0.68$ GeV $\alpha_s = 0.12097 \pm 0.00067$

Table 4.6: A comparison between a subset of our results (last column) and results from other PDF fitting groups. In particular, we compare our results to the work from ABMPtt [47], MSHT [44], and the fixed PDF determination from Ref. [43]. We have indicated the pole-mass and $\overline{\text{MS}}$ mass in superscript, for clarity.

should come as no surprise given that the determination in Ref. [43] ignores the very significant correlations between $\alpha_s(m_Z)$ and the PDFs [48, 49]. Note however that Ref. [43] finds a strong (positive) correlation between α_s and m_t when using observables differential in the rapidity, which is also the observable with the highest degree of correlation in our determination.

5 Summary and outlook

In this work we have presented a determination of the top-quark mass while jointly varying the strong coupling constant within a global PDF analysis. We employed the theory covariance method (TCM), validated in this context using closure tests. We have considered a wide range of single and double differential $t\bar{t}$ cross-section measurements from ATLAS and CMS, taken at 8 and 13 TeV, analysing their individual and combined impact on the joint (α_s, m_t) parameter space. The analysis is performed using NNLO QCD, including MHOU's, complemented with EW corrections, and accounting for PDF evolution up to $\text{aN}^3\text{LO}_{\text{QCD}} \otimes \text{NLO}_{\text{QED}}$. We have analysed, for the first time, the possible impact of toponium corrections on the extraction of the top-quark mass.

Our findings are as follows. First, out of all the kinematic observables that we have considered, we find that double differential measurements in $(m_{t\bar{t}}, y_{t\bar{t}})$ provide the most stringent bounds on m_t , followed by single differential distributions in $m_{t\bar{t}}$ and p_T^t . Observables differential in the top quark rapidity are the least sensitive to m_t . In all cases, limited correlation between α_s and m_t is observed, with the exception of rapidity based

determinations. The central value of m_t is determined rather consistently across all the kinematic observables considered, generally within a standard deviation, and the outliers are observables which do not determine m_t very precisely, and also have a relatively poor χ^2 in the fit.

Our most precise extraction with satisfactory agreement between theory and data originates from the single differential measurements in $m_{t\bar{t}}$: combining all the data from ATLAS and CMS, we find $m_t = 172.29 \pm 0.25$ GeV at NNLO with MHOUs, and $m_t = 172.80 \pm 0.26$ GeV at aN³LO \otimes NLO_{QED} with EW and toponium corrections, both in agreement with the current PDG average [17] and the LHC combination measurement [38]. It is particularly striking that our indirect measurement, by combining a variety of datasets in a fully correlated analysis, is both competitive with, and consistent with, the direct measurements from the kinematics of the final state, while not suffering from the well known Monte Carlo ambiguities inherent in such determinations.

Regarding the impact of perturbative corrections, we find that aN³LO corrections cause a slight downward shift of m_t , while EW corrections push m_t up again by around 0.3 GeV. The overall picture that emerges is that the agreement between results from different observables improves under the addition of these higher order corrections. Toponium corrections have a rather greater impact, increasing m_t by as much as 0.6 GeV in extractions based on $m_{t\bar{t}}$. However m_t instead remains relatively stable in determinations differential in p_T^t or the rapidities y_t and $y_{t\bar{t}}$. As a result, the toponium corrections also improve the mutual consistency across kinematic observables.

Finally, we have explicitly demonstrated how combining individual measurements for the purpose of determining SM quantities requires one to refit the PDFs in order to correctly account for all correlations and avoid double counting. As is well known, a naive statistical a posteriori average underestimates uncertainties, as it ignores correlations, while a PDF4LHC-like combination at the level of replicas significantly overestimates uncertainties, as does an envelope approach. The TCM takes all correlations into account correctly, making it the ideal method for performing such combinations, which is especially relevant when combining existing LHC determinations. Here we also note the benefit one gains once inter-spectra correlations across different observables and hope that these will become more widely available in the future.

The techniques used here can be extended in various directions. It will be interesting to study how particle level, rather than parton level, top production measurements affect the sensitivity to the top mass [113, 114], by determining power corrections to the top cross-section using similar techniques to those recently explored for jets [51].

The TCM methodology can be easily used to perform fully correlated global determinations of additional SM parameters, in particular the W -boson mass and the weak mixing angle $\sin^2 \theta_W$. As is well known, the largest sources of uncertainty in determinations of both these quantities at the LHC are the strong coupling and the PDFs. Moreover the W -boson mass receives radiative corrections sensitive to the top quark's mass, which can therefore introduce a non-trivial interplay [115]. A truly precise global determination will require all these correlations to be properly accounted for.

Beyond this, it will be interesting to attempt to fit, in addition, Wilson coefficients

within the Standard Model Effective Field Theory (SMEFT) framework [116]. This is technically rather straightforward using the TCM, since the dependence of cross-sections on the SMEFT coefficients is easily computed, and any number of correlated coefficients can be determined within a single global PDF fit. Again the key to successful global determinations is to fully account for correlations, both to PDFs and to SM parameters.

Acknowledgments. We would like to thank the members of the NNPDF collaboration for insightful discussions during the course of this work. We are particularly grateful to Tanishq Sharma for his work on the data set implementation and assistance with MATRIX in the early stages of this project, and to Emanuele Nocera for assisting us with the electroweak corrections. J.t.H would like to thank Rafael Aoude and Thomas Cridge for useful discussions, and we would also like to thank Paolo Nason and Luca Rottoli for correspondence on the estimation of the toponium correction. The work of R.D.B, J.t.H and R.S. is supported by the Science and Technology Facilities Council (STFC) via grant awards ST/T000600/1 and ST/X000494/1.

A Toponium k -factors

In this appendix, we present the numerical values of the toponium k -factors that were computed following the procedure outline in Sect. 3.3 for the data sets listed in Table 3.1. Table A.1 shows all the k -factors different from unity in the case of ATLAS measurements, while Table A.2 shows the equivalent values for the CMS measurements.

ATLAS $t\bar{t}$ 13 TeV hadr.			ATLAS $t\bar{t}$ 13 TeV $\ell + j$		
Obs.	bin	$k_i^{(\text{topo})}$	Obs.	bin	$k_i^{(\text{topo})}$
$(m_{t\bar{t}}, y_{t\bar{t}})$	$((0, 700), (0.00, 0.46))$	1.0083	$m_{t\bar{t}}$	$(325.0, 400.0)$	1.0351
	$((0, 700), (0.46, 0.91))$	1.0085	p_T^t	$(0.0, 50.0)$	1.0475
	$((0, 700), (0.91, 1.55))$	1.0089	y_t	$(0.0, 0.4)$	1.0084
	$((0, 700), (1.55, 2.50))$	1.0101		$(0.4, 0.8)$	1.0083
$y_{t\bar{t}}$	$(0.00, 0.12)$	1.0073		$(0.8, 1.2)$	1.0080
	$(0.12, 0.24)$	1.0072		$(1.2, 1.7)$	1.0076
	$(0.24, 0.36)$	1.0071		$(1.7, 2.5)$	1.0068
	$(0.36, 0.49)$	1.0072	$y_{t\bar{t}}$	$(0.0, 0.25)$	1.0072
	$(0.49, 0.62)$	1.0073		$(0.25, 0.5)$	1.0072
	$(0.62, 0.76)$	1.0073		$(0.5, 0.8)$	1.0073
	$(0.76, 0.91)$	1.0076		$(0.8, 1.1)$	1.0075
	$(0.91, 1.06)$	1.0074		$(1.1, 1.4)$	1.0079
	$(1.06, 1.21)$	1.0078		$(1.4, 1.8)$	1.0087
	$(1.21, 1.39)$	1.0079		$(1.8, 2.5)$	1.0104
$(1.39, 1.59)$	1.0085	(p_T, y_t)		$((0.0, 0.75), (0.0, 85.0))$	1.0229
$(1.59, 2.40)$	1.0098			$((0.75, 1.5), (0.0, 85.0))$	1.0213
$m_{t\bar{t}}$	$(325.0, 458.75)$	1.0167			$((1.5, 2.5), (0.0, 85.0))$
ATLAS $t\bar{t}$ 8 TeV 2ℓ .			ATLAS $t\bar{t}$ 8 TeV $\ell + j$.		
Obs.	bin	$k_i^{(\text{topo})}$	Obs.	bin	$k_i^{(\text{topo})}$
$y_{t\bar{t}}$	$(0.0, 0.4)$	1.0082	$m_{t\bar{t}}$	$(345.0, 400.0)$	1.0207
	$(0.4, 0.8)$	1.0084	p_T^t	$(0.0, 60.0)$	1.0364
	$(0.8, 1.2)$	1.0089	y_t	$(0.0, 0.4)$	1.0099
	$(1.2, 2.0)$	1.0099		$(0.4, 0.8)$	1.0096
	$(2.0, 2.8)$	1.0133		$(0.8, 1.2)$	1.0091
$m_{t\bar{t}}$	$(250.0, 450.0)$	1.0184		$(1.2, 1.6)$	1.0080
				$(1.6, 2.5)$	1.0061
			$y_{t\bar{t}}$	$(0.0, 0.3)$	1.0082
				$(0.3, 0.6)$	1.0083
				$(0.6, 0.9)$	1.0085
				$(0.9, 1.3)$	1.0091
				$(1.3, 2.5)$	1.0105

Table A.1: Toponium k-factors for the ATLAS $t\bar{t}$ measurements listed in Table 3.1.

(a) CMS $t\bar{t}$ 13 TeV 2ℓ , 138 fb $^{-1}$

Obs.	bin	$k_i^{(\text{topo})}$
$m_{t\bar{t}}$	(300.0, 380.0)	1.0600
p_T^t	(0.0, 55.0)	1.0403
y_t	(-2.6, -1.8)	1.0063
	(-1.8, -1.35)	1.0075
	(-1.35, -0.9)	1.0081
	(-0.9, -0.45)	1.0081
	(-0.45, 0.0)	1.0084
	(0.0, 0.45)	1.0084
	(0.45, 0.9)	1.0082
	(0.9, 1.35)	1.0079
	(1.35, 1.8)	1.0075
	(1.8, 2.6)	1.0065
$(m_{t\bar{t}}, y_{t\bar{t}})$	((300, 400), (0.0, 0.35))	1.0365
	((300, 400), (0.35, 0.75))	1.0362
	((300, 400), (0.75, 1.15))	1.0358
	((300, 400), (1.15, 2.5))	1.0346

(c) CMS $t\bar{t}$ 13 TeV $\ell + j$

Obs.	bin	$k_i^{(\text{topo})}$
y_t	(0.0, 0.2)	1.0084
	(0.2, 0.4)	1.0084
	(0.4, 0.6)	1.0083
	(0.6, 0.8)	1.0084
	(0.8, 1.0)	1.0080
	(1.0, 1.2)	1.0080
	(1.2, 1.4)	1.0077
	(1.4, 1.6)	1.0076
	(1.6, 1.8)	1.0075
	(1.8, 2.0)	1.0073
(2.0, 2.5)	1.0063	
$m_{t\bar{t}}$	(250.0, 400.0)	1.0350
$y_{t\bar{t}}$	(0.0, 0.2)	1.0073
	(0.2, 0.4)	1.0070
	(0.4, 0.6)	1.0074
	(0.6, 0.8)	1.0073
	(0.8, 1.0)	1.0076
	(1.0, 1.2)	1.0076
	(1.2, 1.4)	1.0080
	(1.4, 1.6)	1.0085
(1.6, 1.8)	1.0090	
(1.8, 2.4)	1.0104	

(b) CMS $t\bar{t}$ 13 TeV 2ℓ

Obs.	bin	$k_i^{(\text{topo})}$
p_T^t	(0.0, 65.0)	1.0305
$m_{t\bar{t}}$	(300.0, 380.0)	1.0600
y_t	(-2.6, -1.8)	1.0063
	(-1.8, -1.35)	1.0075
	(-1.35, -0.9)	1.0081
	(-0.9, -0.45)	1.0081
	(-0.45, 0.0)	1.0084
	(0.0, 0.45)	1.0084
	(0.45, 0.9)	1.0082
	(0.9, 1.35)	1.0079
	(1.35, 1.8)	1.0075
	(1.8, 2.6)	1.0065
$y_{t\bar{t}}$	(-2.6, -1.6)	1.0096
	(-1.6, -1.2)	1.0083
	(-1.2, -0.8)	1.0076
	(-0.8, -0.4)	1.0072
	(-0.4, 0.0)	1.0071
	(0.0, 0.4)	1.0071
	(0.4, 0.8)	1.0073
	(0.8, 1.2)	1.0075
	(1.2, 1.6)	1.0081
	(1.6, 2.6)	1.0099

(d) CMS $t\bar{t}$ 13 TeV $\ell + j$ (continued)

Obs.	bin	$k_i^{(\text{topo})}$
$(m_{t\bar{t}}, y_{t\bar{t}})$	((250.0, 420.0), (0.0, 0.3))	1.0258
	((250.0, 420.0), (0.3, 0.6))	1.0260
	((250.0, 420.0), (0.6, 0.9))	1.0253
	((250.0, 420.0), (0.9, 1.2))	1.0252
	((250.0, 420.0), (1.2, 1.5))	1.0252
	((250.0, 420.0), (1.5, 2.5))	1.0246
p_T^t	(0.0, 40.0)	1.0686
	(40.0, 80.0)	1.0010

Table A.2: Toponium k-factors for the CMS $t\bar{t}$ measurements listed in Table 3.1.

References

- [1] ATLAS collaboration, *Measurement of the $t\bar{t}$ production cross-section in pp collisions at $\sqrt{s} = 5.02$ TeV with the ATLAS detector*, *JHEP* **06** (2023) 138 [2207.01354].
- [2] ATLAS collaboration, *Measurement of the $t\bar{t}$ production cross-section using $e\mu$ events with b -tagged jets in pp collisions at $\sqrt{s} = 7$ and 8 TeV with the ATLAS detector*, *Eur. Phys. J. C* **74** (2014) 3109 [1406.5375].
- [3] ATLAS collaboration, *Measurement of the $t\bar{t}$ production cross-section in the lepton+jets channel at $\sqrt{s} = 13$ TeV with the ATLAS experiment*, *Phys. Lett. B* **810** (2020) 135797 [2006.13076].
- [4] CMS collaboration, *Measurement of the inclusive $t\bar{t}$ cross section in pp collisions at $\sqrt{s} = 5.02$ TeV using final states with at least one charged lepton*, *JHEP* **03** (2018) 115 [1711.03143].
- [5] CMS collaboration, *Measurement of the t -bar production cross section in the e - μ channel in proton-proton collisions at $\sqrt{s} = 7$ and 8 TeV*, *JHEP* **08** (2016) 029 [1603.02303].
- [6] CMS collaboration, *Measurement of the top quark pair production cross section in proton-proton collisions at $\sqrt{s} = 13$ TeV*, *Phys. Rev. Lett.* **116** (2016) 052002 [1510.05302].
- [7] CMS collaboration, *Measurements of $t\bar{t}$ differential cross sections in proton-proton collisions at $\sqrt{s} = 13$ TeV using events containing two leptons*, *JHEP* **02** (2019) 149 [1811.06625].
- [8] ATLAS collaboration, *Measurements of top-quark pair single- and double-differential cross-sections in the all-hadronic channel in pp collisions at $\sqrt{s} = 13$ TeV using the ATLAS detector*, *JHEP* **01** (2021) 033 [2006.09274].
- [9] ATLAS collaboration, *Measurements of top-quark pair differential and double-differential cross-sections in the ℓ +jets channel with pp collisions at $\sqrt{s} = 13$ TeV using the ATLAS detector*, *Eur. Phys. J. C* **79** (2019) 1028 [1908.07305].
- [10] ATLAS collaboration, *Measurement of top quark pair differential cross-sections in the dilepton channel in pp collisions at $\sqrt{s} = 7$ and 8 TeV with ATLAS*, *Phys. Rev. D* **94** (2016) 092003 [1607.07281].
- [11] ATLAS collaboration, *Measurements of top-quark pair differential cross-sections in the lepton+jets channel in pp collisions at $\sqrt{s} = 8$ TeV using the ATLAS detector*, *Eur. Phys. J. C* **76** (2016) 538 [1511.04716].
- [12] CMS collaboration, *Measurement of differential $t\bar{t}$ production cross sections in the full kinematic range using lepton+jets events from proton-proton collisions at $\sqrt{s} = 13$ TeV*, *Phys. Rev. D* **104** (2021) 092013 [2108.02803].
- [13] CMS collaboration, *Measurement of $t\bar{t}$ normalised multi-differential cross sections in pp collisions at $\sqrt{s} = 13$ TeV, and simultaneous determination of the strong coupling strength, top quark pole mass, and parton distribution functions*, *Eur. Phys. J. C* **80** (2020) 658 [1904.05237].
- [14] CMS collaboration, *Differential cross section measurements for the production of top quark pairs and of additional jets using dilepton events from pp collisions at $\sqrt{s} = 13$ TeV*, *JHEP* **02** (2025) 064 [2402.08486].

- [15] CMS collaboration, *First measurement of the top quark pair production cross section in proton-proton collisions at $\sqrt{s} = 13.6$ TeV*, *JHEP* **08** (2023) 204 [[2303.10680](#)].
- [16] ATLAS collaboration, *Measurement of the $t\bar{t}$ cross section and its ratio to the Z production cross section using pp collisions at $s=13.6$ TeV with the ATLAS detector*, *Phys. Lett. B* **848** (2024) 138376 [[2308.09529](#)].
- [17] PARTICLE DATA GROUP collaboration, *Review of particle physics*, *Phys. Rev. D* **110** (2024) 030001.
- [18] A. H. Hoang, *What is the Top Quark Mass?*, *Ann. Rev. Nucl. Part. Sci.* **70** (2020) 225 [[2004.12915](#)].
- [19] GFITTER GROUP collaboration, *The global electroweak fit at NNLO and prospects for the LHC and ILC*, *Eur. Phys. J. C* **74** (2014) 3046 [[1407.3792](#)].
- [20] J. de Blas, M. Ciuchini, E. Franco, A. Goncalves, S. Mishima, M. Pierini et al., *Global analysis of electroweak data in the Standard Model*, *Phys. Rev. D* **106** (2022) 033003 [[2112.07274](#)].
- [21] Z. Kassabov, M. Madigan, L. Mantani, J. Moore, M. Morales Alvarado, J. Rojo et al., *The top quark legacy of the LHC Run II for PDF and SMEFT analyses*, *JHEP* **05** (2023) 205 [[2303.06159](#)].
- [22] E. Celada, T. Giani, J. ter Hoeve, L. Mantani, J. Rojo, A. N. Rossia et al., *Mapping the SMEFT at high-energy colliders: from LEP and the (HL-)LHC to the FCC-ee*, *JHEP* **09** (2024) 091 [[2404.12809](#)].
- [23] A. Andreassen, W. Frost and M. D. Schwartz, *Scale Invariant Instantons and the Complete Lifetime of the Standard Model*, *Phys. Rev. D* **97** (2018) 056006 [[1707.08124](#)].
- [24] G. Degrassi, S. Di Vita, J. Elias-Miro, J. R. Espinosa, G. F. Giudice, G. Isidori et al., *Higgs mass and vacuum stability in the Standard Model at NNLO*, *JHEP* **08** (2012) 098 [[1205.6497](#)].
- [25] F. Bezrukov, M. Y. Kalmykov, B. A. Kniehl and M. Shaposhnikov, *Higgs Boson Mass and New Physics*, *JHEP* **10** (2012) 140 [[1205.2893](#)].
- [26] A. V. Bednyakov, B. A. Kniehl, A. F. Pikelner and O. L. Veretin, *Stability of the Electroweak Vacuum: Gauge Independence and Advanced Precision*, *Phys. Rev. Lett.* **115** (2015) 201802 [[1507.08833](#)].
- [27] CDF collaboration, *Observation of top quark production in $\bar{p}p$ collisions*, *Phys. Rev. Lett.* **74** (1995) 2626 [[hep-ex/9503002](#)].
- [28] D0 collaboration, *Observation of the top quark*, *Phys. Rev. Lett.* **74** (1995) 2632 [[hep-ex/9503003](#)].
- [29] CMS collaboration, *Measurement of the top quark mass in the all-jets final state at $\sqrt{s} = 13$ TeV and combination with the lepton+jets channel*, *Eur. Phys. J. C* **79** (2019) 313 [[1812.10534](#)].
- [30] CMS collaboration, *Measurement of the $t\bar{t}$ production cross section, the top quark mass, and the strong coupling constant using dilepton events in pp collisions at $\sqrt{s} = 13$ TeV*, *Eur. Phys. J. C* **79** (2019) 368 [[1812.10505](#)].
- [31] CMS collaboration, *Measurement of the Jet Mass Distribution and Top Quark Mass in*

- Hadronic Decays of Boosted Top Quarks in pp Collisions at $\sqrt{s} = 13$ TeV*, *Phys. Rev. Lett.* **124** (2020) 202001 [[1911.03800](#)].
- [32] CMS collaboration, *Measurement of the top quark mass using events with a single reconstructed top quark in pp collisions at $\sqrt{s} = 13$ TeV*, *JHEP* **12** (2021) 161 [[2108.10407](#)].
- [33] CMS collaboration, *Measurement of the top quark mass using a profile likelihood approach with the lepton + jets final states in proton–proton collisions at $\sqrt{s} = 13$ TeV*, *Eur. Phys. J. C* **83** (2023) 963 [[2302.01967](#)].
- [34] CMS collaboration, *Measurement of the top quark pole mass using $t\bar{t}$ +jet events in the dilepton final state in proton-proton collisions at $\sqrt{s} = 13$ TeV*, *JHEP* **07** (2023) 077 [[2207.02270](#)].
- [35] ATLAS collaboration, *Measurement of the top-quark mass using a leptonic invariant mass in pp collisions at $\sqrt{s} = 13$ TeV with the ATLAS detector*, *JHEP* **06** (2023) 019 [[2209.00583](#)].
- [36] ATLAS collaboration, *Measurement of the top quark mass with the ATLAS detector using $t\bar{t}$ events with a high transverse momentum top quark*, *Phys. Lett. B* **867** (2025) 139608 [[2502.18216](#)].
- [37] CMS collaboration, *Measurement of the differential $t\bar{t}$ production cross section as a function of the jet mass and extraction of the top quark mass in hadronic decays of boosted top quarks*, *Eur. Phys. J. C* **83** (2023) 560 [[2211.01456](#)].
- [38] ATLAS, CMS collaboration, *Combination of Measurements of the Top Quark Mass from Data Collected by the ATLAS and CMS Experiments at $s=7$ and 8 TeV*, *Phys. Rev. Lett.* **132** (2024) 261902 [[2402.08713](#)].
- [39] ATLAS, CMS collaboration, *Highlights of the HL-LHC physics projections by ATLAS and CMS*, [2504.00672](#).
- [40] FCC collaboration, *Future Circular Collider Feasibility Study Report: Volume 1, Physics, Experiments, Detectors*, [2505.00272](#).
- [41] S. Alekhin, J. Blümlein, S. Moch and R. Placakyte, *Parton distribution functions, α_s , and heavy-quark masses for LHC Run II*, *Phys. Rev. D* **96** (2017) 014011 [[1701.05838](#)].
- [42] M. V. Garzelli, L. Kemmler, S. Moch and O. Zenaiev, *Heavy-flavor hadro-production with heavy-quark masses renormalized in the $\overline{\text{MS}}$, MSR and on-shell schemes*, *JHEP* **04** (2021) 043 [[2009.07763](#)].
- [43] A. M. Cooper-Sarkar, M. Czakon, M. A. Lim, A. Mitov and A. S. Papanastasiou, *Simultaneous extraction of α_s and m_t from LHC $t\bar{t}$ differential distributions*, [2010.04171](#).
- [44] T. Cridge and M. A. Lim, *Constraining the top-quark mass within the global MSHT PDF fit*, *Eur. Phys. J. C* **83** (2023) 805 [[2306.14885](#)].
- [45] M. V. Garzelli, J. Mazzitelli, S. O. Moch and O. Zenaiev, *Top-quark pole mass extraction at NNLO accuracy, from total, single- and double-differential cross sections for $t\bar{t} + X$ production at the LHC*, *JHEP* **05** (2024) 321 [[2311.05509](#)].
- [46] J. Holguin, I. Moulton, A. Pathak, M. Procura, R. Schöfbeck and D. Schwarz, *Using the W Boson as a Standard Candle to Reach the Top: Calibrating Energy-Correlator-Based Top Mass Measurements*, *Phys. Rev. Lett.* **134** (2025) 231903 [[2311.02157](#)].

- [47] S. Alekhin, M. V. Garzelli, S. O. Moch and O. Zenaiev, *NNLO PDFs driven by top-quark data*, *Eur. Phys. J. C* **85** (2025) 162 [2407.00545].
- [48] S. Forte and Z. Kassabov, *Why α_s cannot be determined from hadronic processes without simultaneously determining the parton distributions*, *Eur. Phys. J. C* **80** (2020) 182 [2001.04986].
- [49] S. Forte, J. Rojo and R. Stegeman, *Extractions of the strong coupling from collider data without PDF refitting are biased*, in *2025 European Physical Society Conference on High Energy Physics*, 11, 2025, 2511.22561.
- [50] NNPDF collaboration, *A determination of $\alpha_s(m_Z)$ at $aN^3LO_{QCD} \otimes NLO_{QED}$ accuracy from a global PDF analysis*, *Eur. Phys. J. C* **85** (2025) 1001 [2506.13871].
- [51] R. D. Ball, A. Chiefa and R. Stegeman, *Parton distributions with higher twist and jet power corrections*, 2511.14387.
- [52] R. D. Ball and A. Deshpande, *The proton spin, semi-inclusive processes, and measurements at a future Electron Ion Collider*, published in ‘From My Vast Repertoire ...: Guido Altarelli’s Legacy’, eds A. Levy, S. Forte and G. Ridolfi, pp. 205–226. World Scientific, 2019. 1801.04842. 10.1142/97898132380530011.
- [53] NNPDF collaboration, *Nuclear Uncertainties in the Determination of Proton PDFs*, *Eur. Phys. J. C* **79** (2019) 282 [1812.09074].
- [54] NNPDF collaboration, *Parton Distributions with Theory Uncertainties: General Formalism and First Phenomenological Studies*, *Eur. Phys. J. C* **79** (2019) 931 [1906.10698].
- [55] R. D. Ball and R. L. Pearson, *Correlation of theoretical uncertainties in PDF fits and theoretical uncertainties in predictions*, *Eur. Phys. J. C* **81** (2021) 830 [2105.05114].
- [56] NNPDF collaboration, *The path to proton structure at 1% accuracy*, *Eur. Phys. J. C* **82** (2022) 428 [2109.02653].
- [57] ATLAS collaboration, *Observation of a cross-section enhancement near the $t\bar{t}$ production threshold in $\sqrt{s} = 13$ TeV pp collisions with the ATLAS detector*, .
- [58] CMS collaboration, *Observation of a pseudoscalar excess at the top quark pair production threshold*, *Rept. Prog. Phys.* **88** (2025) 087801 [2503.22382].
- [59] NNPDF collaboration, *Precision determination of the strong coupling constant within a global PDF analysis*, *Eur. Phys. J.* **C78** (2018) 408 [1802.03398].
- [60] NNPDF collaboration, *An open-source machine learning framework for global analyses of parton distributions*, *Eur. Phys. J. C* **81** (2021) 958 [2109.02671].
- [61] NNPDF collaboration, *Parton distributions for the LHC Run II*, *JHEP* **04** (2015) 040 [1410.8849].
- [62] L. Del Debbio, T. Giani and M. Wilson, *Bayesian approach to inverse problems: an application to NNPDF closure testing*, *Eur. Phys. J. C* **82** (2022) 330 [2111.05787].
- [63] L. A. Harland-Lang, T. Cridge and R. S. Thorne, *A stress test of global PDF fits: closure testing the MSHT PDFs and a first direct comparison to the neural net approach*, *Eur. Phys. J. C* **85** (2025) 316 [2407.07944].
- [64] A. Barontini, M. N. Costantini, G. De Crescenzo, S. Forte and M. Ubiali, *Evaluating the faithfulness of PDF uncertainties in the presence of inconsistent data*, 2503.17447.

- [65] S. Devoto, T. Jezo, S. Kallweit and C. Schwan, *MATRIX HAWAII: PineAPPL interpolation grids with MATRIX*, [2506.14486](#).
- [66] M. Grazzini, S. Kallweit and M. Wiesemann, *Fully differential NNLO computations with MATRIX*, *Eur. Phys. J. C* **78** (2018) 537 [[1711.06631](#)].
- [67] S. Carrazza, E. R. Nocera, C. Schwan and M. Zaro, *PineAPPL: combining EW and QCD corrections for fast evaluation of LHC processes*, *JHEP* **12** (2020) 108 [[2008.12789](#)].
- [68] C. Schwan, T. R. Rabemananjara, A. Candido, F. Hekhorn, T. Sharma, S. Carrazza et al., *Nnpdf/pineappl: v1.0.0*, June, 2025. [10.5281/zenodo.15635174](#).
- [69] M. Czakon, Z. Kassabov, A. Mitov, R. Poncelet and A. Popescu, *HighTEA: high energy theory event analyser*, *J. Phys. G* **51** (2024) 115002 [[2304.05993](#)].
- [70] J. Alwall, R. Frederix, S. Frixione, V. Hirschi, F. Maltoni, O. Mattelaer et al., *The automated computation of tree-level and next-to-leading order differential cross sections, and their matching to parton shower simulations*, *JHEP* **07** (2014) 079 [[1405.0301](#)].
- [71] NNPDF collaboration, *Determination of the theory uncertainties from missing higher orders on NNLO parton distributions with percent accuracy*, *Eur. Phys. J. C* **84** (2024) 517 [[2401.10319](#)].
- [72] NNPDF collaboration, *The path to N^3 LO parton distributions*, *Eur. Phys. J. C* **84** (2024) 659 [[2402.18635](#)].
- [73] A. Candido, F. Hekhorn and G. Magni, *EKO: evolution kernel operators*, *Eur. Phys. J. C* **82** (2022) 976 [[2202.02338](#)].
- [74] A. Candido, F. Hekhorn and G. Magni, *Nnpdf/eko: v0.14.6*, June, 2025. [10.5281/zenodo.15655642](#).
- [75] NNPDF collaboration, *Photons in the proton: implications for the LHC*, *Eur. Phys. J. C* **84** (2024) 540 [[2401.08749](#)].
- [76] J. Ablinger, A. Behring, J. Blümlein, A. De Freitas, A. von Manteuffel, C. Schneider et al., *The non-first-order-factorizable contributions to the three-loop single-mass operator matrix elements $AQg(3)$ and $\Delta AQg(3)$* , *Phys. Lett. B* **854** (2024) 138713 [[2403.00513](#)].
- [77] G. Falcioni, F. Herzog, S. Moch, A. Pelloni and A. Vogt, *Four-loop splitting functions in QCD – the gluon-gluon case –*, *Phys. Lett. B* **860** (2025) 139194 [[2410.08089](#)].
- [78] M. Czakon, D. Heymes, A. Mitov, D. Pagani, I. Tsirikos and M. Zaro, *Top-pair production at the LHC through NNLO QCD and NLO EW*, *JHEP* **10** (2017) 186 [[1705.04105](#)].
- [79] B. Fuks, K. Hagiwara, K. Ma and Y.-J. Zheng, *Signatures of toponium formation in LHC run 2 data*, *Phys. Rev. D* **104** (2021) 034023 [[2102.11281](#)].
- [80] B. Fuks, K. Hagiwara, K. Ma and Y.-J. Zheng, *Simulating toponium formation signals at the LHC*, *Eur. Phys. J. C* **85** (2025) 157 [[2411.18962](#)].
- [81] V. S. Fadin and V. A. Khoze, *Threshold Behavior of Heavy Top Production in $e+e-$ Collisions*, *JETP Lett.* **46** (1987) 525.
- [82] V. S. Fadin, V. A. Khoze and T. Sjostrand, *On the Threshold Behavior of Heavy Top Production*, *Z. Phys. C* **48** (1990) 613.
- [83] F. Maltoni, C. Severi, S. Tentori and E. Vryonidou, *Quantum detection of new physics in top-quark pair production at the LHC*, *JHEP* **03** (2024) 099 [[2401.08751](#)].

- [84] Y. Sumino and H. Yokoya, *Bound-state effects on kinematical distributions of top quarks at hadron colliders*, *JHEP* **09** (2010) 034 [[1007.0075](#)].
- [85] M. A. Braun, *Positronium Singularities in Quantum Electrodynamics and Perturbation Theory*, *Sov. Phys. JETP* **27** (1968) 652.
- [86] K. Melnikov, A. Vainshtein and M. Voloshin, *Remarks on the effect of bound states and threshold in $g-2$* , *Phys. Rev. D* **90** (2014) 017301 [[1402.5690](#)].
- [87] M. I. Eides, *Recent ideas on the calculation of lepton anomalous magnetic moments*, *Phys. Rev. D* **90** (2014) 057301 [[1402.5860](#)].
- [88] M. Beneke and P. Ruiz-Femenia, *Threshold singularities, dispersion relations and fixed-order perturbative calculations*, *JHEP* **08** (2016) 145 [[1606.02434](#)].
- [89] P. Nason, E. Re and L. Rottoli, *Spin correlations in $t\bar{t}$ production and decay at the LHC in QCD perturbation theory*, *JHEP* **10** (2025) 149 [[2505.00096](#)].
- [90] CMS collaboration, *Measurement of differential cross sections for the production of top quark pairs and of additional jets in lepton+jets events from pp collisions at $\sqrt{s} = 13$ TeV*, *Phys. Rev. D* **97** (2018) 112003 [[1803.08856](#)].
- [91] FLAVOUR LATTICE AVERAGING GROUP (FLAG) collaboration, *FLAG Review 2024*, [2411.04268](#).
- [92] A. Candido, S. Forte, T. Giani and F. Hekhorn, *On the positivity of \overline{MS} parton distributions*, *Eur. Phys. J. C* **84** (2024) 335 [[2308.00025](#)].
- [93] S. Bailey and L. Harland-Lang, *Differential Top Quark Pair Production at the LHC: Challenges for PDF Fits*, *Eur. Phys. J. C* **80** (2020) 60 [[1909.10541](#)].
- [94] R. D. Ball, S. Forte and R. Stegeman, *Correlation and combination of sets of parton distributions*, *Eur. Phys. J. C* **81** (2021) 1046 [[2110.08274](#)].
- [95] J. Butterworth et al., *PDF4LHC recommendations for LHC Run II*, *J. Phys. G* **43** (2016) 023001 [[1510.03865](#)].
- [96] M. L. Czakon et al., *Top quark pair production at complete NLO accuracy with NNLO+NNLL' corrections in QCD*, *Chin. Phys. C* **44** (2020) 083104 [[1901.08281](#)].
- [97] J. C. Collins and R. K. Ellis, *Heavy Quark Production in Very High-Energy Hadron Collisions*, *Nucl. Phys. B* **360** (1991) 3.
- [98] R. D. Ball and R. K. Ellis, *Heavy quark production at high-energy*, *JHEP* **05** (2001) 053 [[hep-ph/0101199](#)].
- [99] F. Silveti and M. Bonvini, *Differential heavy quark pair production at small x* , *Eur. Phys. J. C* **83** (2023) 267 [[2211.10142](#)].
- [100] C. Muselli, M. Bonvini, S. Forte, S. Marzani and G. Ridolfi, *Top Quark Pair Production beyond NNLO*, *JHEP* **08** (2015) 076 [[1505.02006](#)].
- [101] C. McNeile, C. T. H. Davies, E. Follana, K. Hornbostel and G. P. Lepage, *High-Precision c and b Masses, and QCD Coupling from Current-Current Correlators in Lattice and Continuum QCD*, *Phys. Rev. D* **82** (2010) 034512 [[1004.4285](#)].
- [102] B. Chakraborty, C. T. H. Davies, B. Galloway, P. Knecht, J. Koponen, G. C. Donald et al., *High-precision quark masses and QCD coupling from $n_f = 4$ lattice QCD*, *Phys. Rev. D* **91** (2015) 054508 [[1408.4169](#)].

- [103] ALPHA collaboration, *Determination of $\alpha_s(m_Z)$ by the non-perturbative decoupling method*, *Eur. Phys. J. C* **82** (2022) 1092 [2209.14204].
- [104] P. Petreczky and J. H. Weber, *Strong coupling constant from moments of quarkonium correlators revisited*, *Eur. Phys. J. C* **82** (2022) 64 [2012.06193].
- [105] C. Ayala, X. Lobregat and A. Pineda, *Determination of $\alpha(M_Z)$ from an hyperasymptotic approximation to the energy of a static quark-antiquark pair*, *JHEP* **09** (2020) 016 [2005.12301].
- [106] TUMQCD collaboration, *Determination of the QCD coupling from the static energy and the free energy*, *Phys. Rev. D* **100** (2019) 114511 [1907.11747].
- [107] S. Cali, K. Cichy, P. Korcyl and J. Simeth, *Running coupling constant from position-space current-current correlation functions in three-flavor lattice QCD*, *Phys. Rev. Lett.* **125** (2020) 242002 [2003.05781].
- [108] ALPHA collaboration, *QCD Coupling from a Nonperturbative Determination of the Three-Flavor Λ Parameter*, *Phys. Rev. Lett.* **119** (2017) 102001 [1706.03821].
- [109] PACS-CS collaboration, *Precise determination of the strong coupling constant in $N_f = 2+1$ lattice QCD with the Schrödinger functional scheme*, *JHEP* **10** (2009) 053 [0906.3906].
- [110] K. Maltman, D. Leinweber, P. Moran and A. Sternbeck, *The Realistic Lattice Determination of $\alpha(s)(M(Z))$ Revisited*, *Phys. Rev. D* **78** (2008) 114504 [0807.2020].
- [111] S. Bailey, T. Cridge, L. A. Harland-Lang, A. D. Martin and R. S. Thorne, *Parton distributions from LHC, HERA, Tevatron and fixed target data: MSHT20 PDFs*, *Eur. Phys. J. C* **81** (2021) 341 [2012.04684].
- [112] NNPDF collaboration, *Parton distributions from high-precision collider data*, *Eur. Phys. J. C* **77** (2017) 663 [1706.00428].
- [113] ATLAS collaboration, *Inclusive and differential cross-sections for dilepton $t\bar{t}$ production measured in $\sqrt{s} = 13$ TeV pp collisions with the ATLAS detector*, *JHEP* **07** (2023) 141 [2303.15340].
- [114] ATLAS collaboration, *Precise measurement of the $t\bar{t}$ production cross-section and lepton differential distributions in $e\mu$ dilepton events from $\sqrt{s} = 13$ TeV pp collisions with the ATLAS detector*, 2509.15066.
- [115] J. de Blas, M. Pierini, L. Reina and L. Silvestrini, *Impact of the Recent Measurements of the Top-Quark and W-Boson Masses on Electroweak Precision Fits*, *Phys. Rev. Lett.* **129** (2022) 271801 [2204.04204].
- [116] E. Cole, M. N. Costantini, E. Hammou, L. Mantani, F. Merlotti, M. Morales-Alvarado et al., *Tailored PDFs for New Physics searches*, 2602.20235.